RSC Advances

ROYAL SOCIETY
OF CHEMISTRY

PAPER

View Article Online
View Journal | View Issue

Check for updates

Cite this: *RSC Adv.*, 2026, **16**, 26399

Synthesis, molecular modelling, and evaluation of new mono- and bis-isoxazolines as antibacterial agents: *in vitro* and *in silico* analysis

Ali Altharawi,[a] Bharath Kumar Chagaleti,*[b] Mubarak A. Alamri,[a] Yassine Riadi,[a] Taibah Aldakhil,[a] Ait Itto Moulay Youssef,[c] Ali Oubella[d] and Reda A. Haggam*[e]

Received 22nd December 2025
Accepted 7th May 2026

DOI: 10.1039/d5ra09902a

rsc.li/rsc-advances

This study aimed to design, synthesize, and evaluate a novel series of isoxazoline-thiosemicarbazone derivatives as potential antibacterial agents, supported by computational investigations. Compounds were synthesized and characterized using ^{1}H and ^{13}C NMR and HRMS. Compounds **4a–d** and **6** were evaluated for their *in vitro* antibacterial activity against Gram-positive and Gram-negative bacterial strains by determining their minimum inhibitory concentrations (MICs). Molecular docking studies were conducted to assess binding interactions with the PTGS2 protein, followed by molecular dynamics simulations to evaluate the stability of the ligand–protein complexes. MM-GBSA calculations were performed to estimate binding free energies, and *in silico* ADMET predictions were carried out to assess drug-likeness. Compounds **4a–d** and **6** exhibited potent antibacterial activity, with MIC values ranging from 0.31 to 0.5 μg mL^{-1}. Molecular docking results revealed strong binding affinities of compound **4a** toward the active site of PTGS2. Molecular dynamics confirmed the structural stability of the PTGS2-**4a** complex. MM-GBSA analysis demonstrated that PTGS2-**4a** displayed the most favorable binding free energy, showing superior or comparable performance to the reference inhibitor Resatorvid. *In silico* ADME-T analysis indicated acceptable pharmacokinetic properties. These results highlight compounds **4a–d** as promising antibacterial candidates, providing a strong rationale for the development of novel isoxazoline-thiosemicarbazone-based antibacterial agents.

1 Introduction

Infectious diseases, predominantly caused by pathogenic bacteria, continue to pose a critical threat to global public health.[1] Although antibiotic therapy remains the cornerstone of bacterial infection management, the widespread emergence of multidrug-resistant (MDR) strains arising from spontaneous genetic mutations or the misuse and overuse of antimicrobial agents has significantly compromised treatment efficacy.[2,3] This growing resistance not only limits the therapeutic arsenal but also contributes to elevated morbidity and mortality rates worldwide.[4,5] Consequently, the urgent need for the discovery and development of novel antibacterial agents, particularly those with innovative mechanisms of action capable of circumventing existing resistance pathways, is increasingly recognized by the scientific community.

In recent decades, heterocyclic scaffolds have gained considerable attention as promising frameworks in the search for novel therapeutic agents to combat the growing challenge of antibiotic resistance.[6] Among them, oxygen- and nitrogen-containing heterocycles are of particular interest due to their widespread occurrence in natural products and pharmacologically active compounds.[7] Importantly, these heterocyclic motifs are frequently embedded in the chemical structures of numerous antimicrobial agents currently used in clinical practice.[8]

In this context, isoxazolines represent a significant class of heterocyclic compounds commonly encountered in a diverse array of both naturally occurring and synthetically derived substances, with applications spanning multiple scientific domains.[9] The isoxazoline core represents a crucial pharmacophoric element found in numerous bioactive agents (Fig. 1-A).[10] Isoxazolines have been reported to exhibit a wide spectrum of pharmacological activities, including anti-inflammatory,[11] anticancer,[12] antifungal,[13] antibacterial,[14] antioxidant,[15] and

---

[a] *Department of Pharmaceutical Chemistry, College of Pharmacy, Prince Sattam Bin Abdulaziz University, Al-Kharj 11942, Saudi Arabia*

[b] *Department of Pharmaceutical Chemistry, SRM College of Pharmacy, Faculty of Medicine and Health Sciences, SRM Institute of Science and Technology, Kattankulathur, Chengalpattu, Chennai 603203, India. E-mail: chagalek@srmist.edu.in*

[c] *Laboratory of Organic Synthesis and Physico-Molecular Chemistry, Department of Chemistry, Faculty of Sciences Semlalia, Université Cadi Ayyad, BP PO Box 2390, Marrakech 40001, Morocco*

[d] *Laboratory of Organic & Physical Chemistry, Applied Bioorganic Chemistry Team, Faculty of Sciences, Ibn Zohr University, Agadir, Morocco*

[e] *Department of Chemistry, Faculty of Science, Islamic University of Madinah, 42351 Madinah, Saudi Arabia. E-mail: relhaggan@iu.edu.sa*

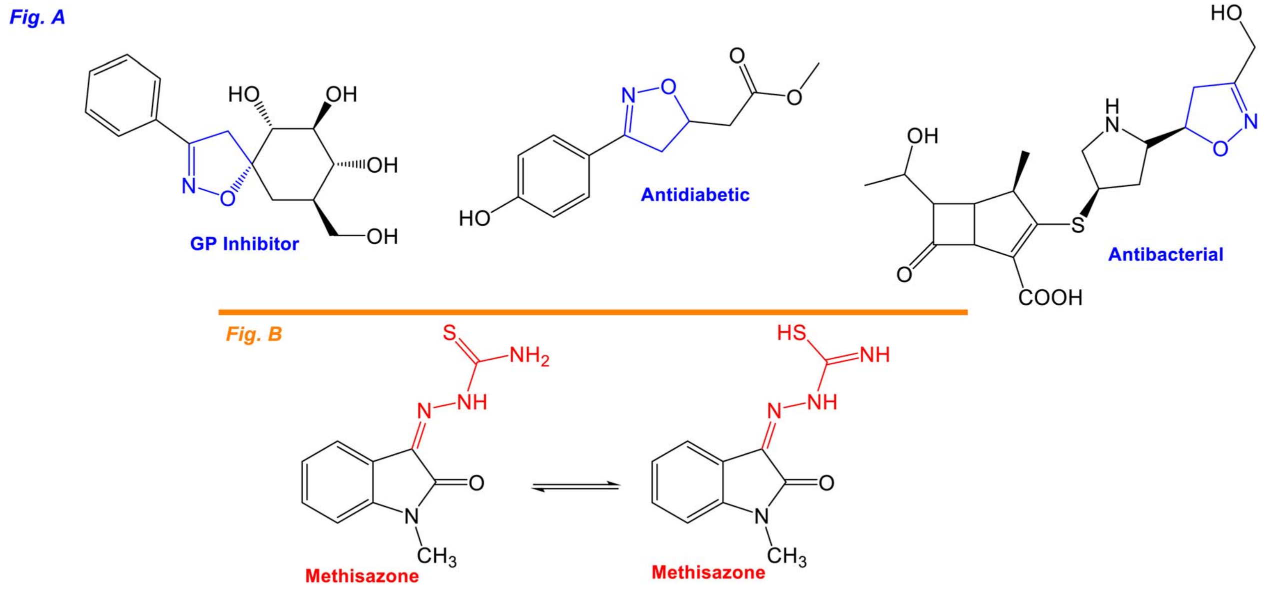

Fig. 1 Representative bioactive compounds incorporating the isoxazoline and thiosemicarbazone scaffold. (A) Inhibitors containing isoxazolines moiety; (B) thiosemicarbazone fused isatin moiety – methisazone.

hypoglycemic effects.[16] The inherent structural versatility of this scaffold renders it highly valuable for the rational design and optimization of novel therapeutic candidates.

Thiosemicarbazone derivatives incorporating an isatin moiety exhibit a broad spectrum of biological activities, including antiviral, antibacterial, anticancer, anticonvulsant, and antidepressant properties.[17,18] Among these, thiosemicarbazones have been widely explored for their potent antiviral activity, particularly their inhibitory effects on the replication of poxviruses.[19,20] A prominent example is methisazone, which has been employed prophylactically since at least 1965.[21] Methisazone (Fig. 1-B), recognized as one of the earliest synthetic antiviral agents used in clinical settings for the treatment of smallpox,[22] exerts its activity by suppressing mRNA and protein synthesis in poxviruses. Additionally, it has demonstrated efficacy against other viral families, including adenoviruses, herpesviruses, picornaviruses, reoviruses, arboviruses, myxoviruses, paramyxoviruses, and retroviruses.[23] Moreover, certain isatin-based compounds have also been reported to possess antifungal and anti-mycotoxin activities.[24]

The rational design of the synthesized compounds is founded on the molecular hybridization strategy, an established approach in medicinal chemistry that involves the covalent integration of two or more distinct pharmacophores into a single molecular framework. This design aims to achieve synergistic biological effects, enhance binding affinity, and potentially circumvent existing resistance mechanisms by targeting multiple pathways simultaneously. Specifically, the isoxazoline ring was selected as a core scaffold due to its rigidity and its proven ability to establish key hydrogen-bonding and hydrophobic interactions within bacterial targets.

Given the favorable pharmacological profiles of both thiosemicarbazone and isoxazoline scaffolds, their incorporation into a single molecular framework is anticipated to generate new heterocyclic entities with enhanced biological potential. In line with our ongoing efforts to develop of therapeutically relevant heterocyclic systems,[25] the present study describes the synthesis and comprehensive structural characterization of novel hybrid molecules featuring both thiosemicarbazone and isoxazoline moieties. These conjugates were obtained *via* a 1,3-dipolar cycloaddition (1,3-DC) strategy. The antibacterial properties were subsequently evaluated *in vitro* against a panel of Gram-positive and Gram-negative bacterial strains. To rationalize the observed biological activities, complementary *in silico* studies were performed, including molecular docking analyses, molecular dynamics (MD) simulations, and ADME-T predictions.

2 Materials and methods

All reagents and solvents employed in this investigation were purchased from commercial suppliers (Sigma-Aldrich) and used as received, without additional purification. TLC was performed on silica gel 60 F_{254} pre-coated plates (0.25 mm thickness, Merck) to monitor reaction progress. Melting points were determined using a Cintex apparatus and are presented uncorrected. Nuclear magnetic resonance (NMR) spectra were recorded on a 300 MHz spectrometer for 1H and 75 MHz for ^{13}C nuclei, using $CDCl_3$ as both solvent. High-resolution mass spectrometry (HRMS) data were acquired on a JEOL JMC-300 instrument operating in electrospray ionization (ESI) mode at 70 eV. It is important to note that intermediate **3** was previously synthesized and fully characterized using spectroscopic techniques, as detailed in our earlier publication.[26]

2.1 Synthesis of mono-isoxazoline 4

Compounds **4a–d** were synthesized *via* a condensation reaction between equimolar amounts (1 mmol) of thiosemicarbazide and the previously obtained intermediates **3a–d** in 30 mL of ethanol. A catalytic amount of concentrated sulfuric acid was added to promote the reaction, and the mixture was refluxed at 90 °C for 6 h. After completion, the reaction mixture was cooled to room temperature, subjected to aqueous workup, and the crude product was purified by column chromatography using hexane/ethyl acetate (82 : 18, v/v) as the eluent.

2.1.1 2-(2-Methyl-5-(5-methyl-3-phenyl-4,5-dihydroisoxazol-5-yl)cyclohex-2-en-1-ylidene)hydrazine-1-carbothioamide 4a. Yield = 80%; solid, mp. = 127± °C; ^{1}H-NMR: 1.4 (s, 3H, CH_3), 1.8 (s, 3H, CH_3), 1.9 (m, 1H, CH), 3.00–2.89 (m, 4H, CH_2), 3.01–3.40 (2d J = 16.7, 2H, $CH_{2oxazole}$), 6.20 (m, 1H, =CH), 6.5 (s, 2H, NH_2), 7.4 (m, 3H, Ar–H), 7.6 (m, 2H, Ar–H), 8.9 (s, 1H, NH); ^{13}C-NMR: 17.8 (CH_3), 23.5 (CH_3), 25.7 (CH_2), 26.2 (CH_2), 41.8 (CH), 43.6 (CH_2), 88.4 (C=), 126.6, 128.8, 129.7, 130.2 (C_{Ar}), 132.3 (CH), 134.5 (C), 149.1 (C), 155.8 (C), 179.1 (C); HRMS $[M + H]^+$, found 343.1592 and calculated 343.1593 (Fig. 1s–4s).

2.1.2 2-(2-Methyl-5-[5-methyl-3-(*p*-tolyl)-4,5-dihydroisoxazol-5-yl]cyclohex-2-en-1-ylidene)hydrazine-1-carbothioamide 4b. Yield 78%; solid; m.p. 121 °C; ^{1}H-NMR: 1.44 (3H, s, CH_3); 1.85 (3H, s, CH_3); 1.90–2.40 (4H, m, 2 × CH_2); 2.37 (3H, s, CH_3); 2.75–2.90 (1H, m, CH); 3.00–3.30 (2H, 2d J = 16.75 Hz, CH_2); 6.20 (1H, m, =C); 6.44 (2H, s, 2NH); 7.20–7.52 (4H, m, HCAr); 8.90 (1H, s, SH). ^{13}C-NMR: 17.8 (CH_3); 21.5 (CH_3); 23.4 (CH_3); 25.67 (CH_2); 26.3 (CH_2); 41.90 (CH); 43.8 (CH_2); 88.1 (C); 126.5 (HCAr); 126.9 (C); 129.5 (HCAr); 132.3 and 132.4 (C); 134.8 (HC=); 140.4 (C); 149.1 (C); 155.8 (C); 179.1 (C). HRMS $[M + H]^+$, found 357.1749, calculated 357.1749 (Fig. 5s–8s).

2.1.3 2-(5-[3-(4-Chlorophenyl)-5-methyl-4,5-dihydroisoxazol-5-yl]-2-methylcyclohex-2-en-1-ylidene)hydrazine-1-carbothioamide 4c. Yield 76%; solid; m.p. 134 °C; ^{1}H-NMR: 1.45 (3H, s, CH_3); 1.85 (3H, s, CH_3); 1.90–2.12 (2H, m, CH_2); 2.30–2.90 (2H, m, CH_2); 2.15–2.25 (1H, m, CH); 3.95–3.30 (2H, 2d J = 16.70 Hz, CH_2); 6.20 (1H, m, HC=); 6.50 (2H, s, 2NH); 7.37–7.58 (4H, m, HCAr); 8.95 (1H, s, SH). ^{13}C-NMR: 17.83 (CH_3); 23.5 (CH_3); 25.7 (CH_2); 26.3 (CH_2); 41.8 (CH); 43.7 (CH_2); 88.8 (C); 127.8 (HCAr); 128.2 (C); 129.1 (HCAr); 132.4 (C); 134.4 (HC=); 136.1 (C); 149.0 (C); 154.9 (C); 179.1 (C). HRMS $[M + H]^+$, found 377.1203, calculated 377.1203 (Fig. 9s–12s).

2.1.4 2-(5-[3-(4-Nitrophenyl)-5-methyl-4,5-dihydroisoxazol-5-yl]-2-methylcyclohex-2-en-1-ylidene)hydrazine-1-carbothioamide 4d. Yield 79%; solid; m.p. 114 °C; ^{1}H-NMR: 1.46 (3H, 2s, CH_3); 1.84 (3H, s, CH_3); 1.90–2.12 (2H, m, CH_2); 2.30–2.90 (2H, m, CH_2); 2.15–2.25 (1H, m, CH); 3.10–3.50 (2H, 2d J = 16.28 Hz, CH_2); 6.20 (1H, m, HC=); 6.57 (2H, s, 2NH); 6.95–7.80 (4H, m, HCAr); 8.93 (1H, s, SH). ^{13}C-NMR: 17.8 (CH_3); 23.5 (CH_3); 25.7 (CH_2); 26.3 (CH_2); 41.6 (CH); 43.4 (CH_2); 88.8 (C); 127.5 (HCAr); 128.2 (C); 129.1 (HCAr); 132.4 (C); 134.4 (HC=); 136.1 (C); 149.0 (C); 154.9 (C); 179.1 (C). HRMS $[M + H]^+$, found 373.1705, calculated 373.1698 (Fig. 3s–15s).

2.2 Synthesis of bis-isoxazoline 5

Compound **5** was synthesized *via* a [3 + 2] cycloaddition reaction between the oxime-derived dipole **2** (2 mmol) and the previously obtained intermediate **3** (1 mmol). The reactants were dissolved in 25 mL of dichloromethane and cooled to 0 °C. A solution of sodium hypochlorite (NaOCl, 25 mL) was then added dropwise over 30 min with continuous stirring. After completion, the reaction mixture was subjected to a standard aqueous workup, and the crude product was purified by column chromatography using hexane/ethyl acetate (80 : 20, v/v) as the eluent.

2.2.1 7*a*-Methyl-5-(5-methyl-3-phenyl-4,5dihydroisoxazol-5-yl)3-phenyl-3*a*,5,6,7*a*-tetrahydrobenzo[*d*]isoxazol-7(4*H*)-one 5. Yield = 31%; solid, mp. = 101 ± 2 °C; ^{1}H-NMR: 1.3 (s, 3H, CH_3), 1.4 (s, 3H, CH_3), 1.5 (m, 1H, CH), 1.9–2.2 (2m, 2H, CH_{2carv}), (m, 1H), 2.4–2,6 (2m, 2H, CH_{2carv}), 2.8–3.1 (m, 2H, $CH_{2oxazole}$), 3.8 (m, 1H, $CH_{2oxazole}$), 7.25–7.55 (m, 6H, Ar–H), 7.56 (m, 2H, Ar–H), 7.69 (m, 2H, Ar–H). ^{13}C-NMR: 20.0 (CH_3), 24.4 (CH_3), 25.5 (CH_2), 38.9 (CH), 39.2 (CH_2), 43.3 (CH_2), 55.5 (CH), 87.7 (C–O), 88.1 (C), 126.5, 127.3, 127.7, 128.8, 129.2, 129.5, 130.2, 136.7 (C_{Ar}), 155.6 (C=N), 158.9 (C=N), 205.0 (C=O). (HRMS $[M + H]^+$), found 389.1859 and calculated 389.1853 (Fig. 16s–18s).

2.3 Synthesis of semicarbazone 6

Compound **6** was prepared *via* condensation synthesized reaction involving equimolar amounts (1 mmol) of thiosemicarbazide and the previously intermediate **5** in 30 mL of ethanol. A catalytic quantity of concentrated sulfuric acid was added to promote the reaction. The mixture was refluxed at 90 ° C for 6 h, and the reaction progress was monitored by TLC. Upon completion, the reaction mixture was cooled to room temperature, subjected to aqueous workup, and the crude product was subsequently purified by column chromatography using a hexane/ethyl acetate (73 : 27, v/v) as the eluent.

2.3.1 2-((7*a*-Methyl-5-(5-methyl-3-phenyl-4,5-dihydroisoxazol-5-yl)-3-phenyl-3*a*,5,6,7*a*-tetrahydrobenzo[*d*]isoxazol-7(4*H*)-ylidene)hydrazine-1-carbothioamide) 6. Yield = 78%; solid, mp. = 115 ± 2 °C; ^{1}H-NMR: 1.2 (s, 3H, CH_3), 1.5 (s, 3H, CH_3), 1.5–1.75 (m, 8H, CH_{2carv} and $CH_{2oxazole}$), 6.5 (s, 2H, NH_2), 7.2–8.5 (m, 10H, Ar–H), 9.2 (s, 1H, NH); ^{13}C-NMR: 22.3 (CH_3), 23.3 (CH_3), 25.8 (CH_2), 36.9 (CH), 37.9 (C H_2), 43.2 (CH_2), 53.3 (CH), 87.2 (C–O), 88.0 (C), 126.4, 126.5, 127.0, 127.9, 128.4, 128.7, 129.1, 129.5, 130.1, 130.5 (C_{Ar}), 148.4 (C=N), 155.7 (C=N)), 178.1 (C=S); (HRMS $[M + H]^+$), found 462.1905 and calculated 462.1996 (Fig. 19s–21s).

2.4 Antibacterial activity

2.4.1 Preparation of the inoculum. Bacterial growth was carried out on Müller–Hinton Agar (MHA) medium, and the cultures were incubated at 37 °C for 24 hours, following the procedure described by Celiktas *et al.*[27] After incubation, the cell density was adjusted to 10^6 cells per mL, including a specific positive control (antibiotic) for each bacterial strain (Table 1).

2.4.2 Microdilution tests: minimum inhibitory concentration (MIC). Determination of the MIC is essential to evaluate the antimicrobial potential of our synthetic products. The assay was performed in a 96-well microplate using the liquid microdilution method described by Pellegrini *et al.*,[28] with some modifications. The products were dissolved in 2% (v/v) DMSO to obtain an initial concentration of 20 μmol mL^{-1}. Aliquots of 10 μL of microbial inoculum, previously adjusted to 10^6 cells per

Table 1 The bacteria used in the study of antibacterial activity and the antibiotics used

Name of the bacteria	Gram	ATCC	Pathogenic effect	Control + (antibiotic)
Pectobacterium carotovorum	Negative	B1158T	Soft rot of various plants and black leg of potato	Ciprofloxacine
Escherichia coli	Negative	8739	Diarrhea, gastroenteritis, urinary tract infections, meningitis, septicemia	Ciprofloxacine
Pseudomonas aeruginosa	Negative	15 442	Nosocomial infections	Renewable energy
Staphylococcus aureus	Positive	6538	Skin and soft tissue infections, pneumonia, endocarditis and osteomyelitis	(Co-trimoxazole)

mL, were added to each well containing 100 μL of serial dilutions of the products. Well 11 (positive control) contained 10 μL of the culture medium and 100 μL of microbial suspension, while well 12 (negative control) contained 100 μL of broth with 2% DMSO and 10 μL of microbial suspension. After preparation, the microplate was incubated at 37 °C for 20 hours. Subsequently, 20 μL of 0.7% aqueous 2,3,5-triphenyl tetrazolium chloride (MTT) was added to each well, and then the plate was incubated again for 4 hours. The MIC was defined as the lowest concentration of product that does not induce any microbial growth, which is reflected by the absence of color change.

3 *In silico* studies

3.1 Network pharmacology

3.1.1 Target screening for designed isoxazole-fused thiosemicarbazide scaffold 4a and 6. To investigate the antibacterial properties of the isoxazole-fused thiosemicarbazide scaffold **4a** and **6**, a network pharmacology-based approach was employed to identify their potential molecular targets and associated biological pathways. The analysis began by submitting the SMILES representations of these new molecules to the SwissTarget Prediction tool to estimate possible human protein targets. These initial predictions were refined using gene relevance scoring to prioritize the most likely targets. To focus the study on antibacterial mechanisms, disease-associated gene data were retrieved from the GeneCards database, and only genes with high relevance scores were selected for further analysis. The intersection between the predicted protein targets and infection-related genes was then computed, and the overlapping set was visualized with a Venn diagram to highlight shared targets.[29–31]

To elucidate the biological context of these core genes, functional enrichment analyses were conducted using the DAVID (Database for Annotation, Visualization, and Integrated Discovery) online tool. Gene Ontology (GO) classification allowed categorisation into three domains: Biological Processes (BP), Molecular Functions (MF), and Cellular Components (CC). Concurrently, Kyoto Encyclopedia of Genes and Genomes (KEGG) pathway analysis identified key signalling pathways modulated by the compounds. Only terms and pathways with adjusted p-values ≤ 0.05 were considered statistically significant. The top ten genes with the strongest enrichment factor were selected for further interpretation regarding their role in antibacterial activity.[32]

A compound-gene interaction network was constructed using Cytoscape (version 3.10.0), where nodes represented either compounds or genes, and the edges indicated their interactions. Genes with high connectivity values were regarded as central to the network's antibacterial action. A protein–protein interaction (PPI) network was developed using STRING, and the topological importance of each node was assessed using the CytoHubba plugin in Cytoscape. Central hub genes were identified based on parameters such as degree and betweenness centrality, marking them as potent targets necessary for the antibacterial effects.[33,34]

3.2 Physicochemical properties

The drug-likeness and oral bioavailability potential of the synthesized isoxazole-fused thiosemicarbazide derivatives were evaluated by analyzing their key physicochemical properties. Parameters such as the octanol–water partition coefficient ($\log P$), molecular weight, number of hydrogen bond donors (HBD), number of hydrogen bond acceptors (HBA), and topological polar surface area (TPSA) were considered. These properties were interpreted based on Lipinski's Rule of Five, where compounds are likely to be orally bioavailable if they have a $\log P$ of ≤ 5, a molecular weight ≤ 500 Da, no more than 5 hydrogen bond donors, and no more than 10 hydrogen bond acceptors. Deviations from these criteria were noted, as they may indicate potential limitations in oral absorption or permeability. The 2D molecular structures of the synthesised compounds were drawn using ChemDraw software. These structures were then uploaded to the Molinspiration tool (https://www.molinspiration.com) to compute the relevant physicochemical descriptors required for drug-likeness evaluation.[35]

3.3 ADME properties

Analyzing ADME parameters is essential for understanding the pharmacokinetic and pharmacodynamic behavior of compounds within the human body. Incorporating ADME predictions early in the drug development pipeline provides a strategic advantage by reducing both time and cost, while also identifying compounds with undesirable properties such as poor bioavailability or potential toxicity, which often lead to late-stage clinical failure. The ADME properties of the new isoxazole-fused thiosemicarbazide derivatives were evaluated using SwissADME, an online computational tool developed by the Swiss Institute of Bioinformatics. This platform applies the SMILES representations of compounds to predict a broad range of pharmacokinetic attributes. The key parameters assessed included lipophilicity ($\log P$), aqueous solubility, gastrointestinal (GI) absorption, and blood–brain barrier (BBB) permeability.[36]

3.4 Toxicity

Toxicological evaluation is an important aspect of the early-phase drug development process, aimed at identifying compounds with potential safety concerns before advancing to clinical studies. Advances in computational toxicology, particularly through the application of machine learning and the availability of curated toxicological datasets, have improved the predictive accuracy of *in silico* tools. In the present study, the toxicity profiles of the synthesized isoxazole-fused thiosemicarbazide derivatives were assessed using ProTox-3.0, an online prediction tool. This tool employs a combination of machine learning models and structural similarity assessments to forecast multiple toxicological endpoints. The SMILES codes of the compounds were submitted, which generated probabilistic scores indicating the likelihood of various toxic effects, including hepatotoxicity, carcinogenicity, immunotoxicity, mutagenicity, and cytotoxicity. The resulting toxicity predictions provided a broad overview of potential safety risks, supporting the prioritization of compounds for further development.[37]

3.5 Molecular docking

Molecular docking was employed to explore the interaction potential between the new isoxazole-fused thiosemicarbazide derivatives and their biological target, using AutoDock 4.2 software. The ligand structures were initially generated from SMILES using UCSF Chimera, in three-dimensional conformations. Energy minimization was then performed to obtain stable geometries in PDB format, suitable for docking analysis. Based on prior network pharmacology results, Cyclooxygenase-2 (COX-2, also known as PTGS2) was selected as the target protein for docking studies. The crystal structure of human COX-2 (PDB ID: 5IKQ, resolution 2.41 Å) was downloaded from the RCSB Protein Data Bank. Protein preparation involved standard procedures such as removal of crystallographic water molecules, addition of polar hydrogen atoms, and assignment of Kollman charges to ensure accurate representation of atomic interactions. The processed protein structure was then saved in PDBQT format with specified rotatable bonds and torsion parameters.

A docking grid was defined to encompass the active site region of COX-2, ensuring proper exposure of the binding pocket. The grid parameter file (.gpf) and docking parameter file (.dpf) were prepared using AutoDock Tools. Docking simulations were executed *via* the command-line interface utilizing the Lamarckian Genetic Algorithm, which generated docking log files (.dlg) containing binding energy scores and predicted ligand orientations. Post-docking analyses were conducted using BIOVIA Discovery Studio Visualizer, enabling analysis of binding poses and interactions. Both 2/3D molecular interaction diagrams were constructed to interpret key contacts such as hydrogen bonds, hydrophobic interactions, and π-stacking within the target binding site.[38–42]

3.6 Molecular dynamics

To gain insights into the conformational stability and dynamic behaviour of the protein–ligand complex, molecular dynamics (MD) simulations were conducted using Desmond v5.9, developed by Schrodinger and academic liscence provided by D. E. Shaw Research Group. The prepared complex was positioned within an orthorhombic simulation box filled with TIP3P water molecules, ensuring a minimum buffer distance of 10 Å between the solute and the box edges to achieve proper solvation. The OPLS (Optimised Potentials for Liquid Simulations) force field was employed to define the interactions among atoms.

System neutrality was achieved by introducing the appropriate number of Na^+ and Cl^- ions. Energy minimisation was subsequently performed using the OPLS-2005 force field to resolve steric clashes and optimise the geometry. Following minimisation, the system underwent equilibration under the NVT ensemble at a starting temperature of 10 K, with temperature regulation managed by the Berendsen thermostat. This was succeeded by a 100-nanosecond production run under NPT conditions, maintaining the temperature at 300 K and pressure at 1 atm. Thermal and pressure control during this phase was ensured using the Nosé–Hoover chain thermostat and the Martyna–Tobias–Klein barostat, respectively.

Throughout the simulation, relaxation steps were applied at 20-picosecond intervals to maintain equilibrium. The resulting trajectory data were processed using the Simulation Interaction Diagram (SID) tools within Desmond. Key analyses included evaluation of root mean square deviations (RMSD), root mean square fluctuations (RMSF), conformational transitions, and persistent molecular interactions between the ligand and the protein. These parameters provided valuable insight into the binding stability, interaction consistency, and structural adaptability of the complex over the simulation period.[43,44]

3.7 MM-GBSA

The Molecular Mechanics Generalized Born Surface Area (MM-GBSA) approach was utilized to estimate the binding affinity and energetic stability of the protein–ligand complex. Calculations were carried out within the Maestro (version 12.3) interface using the OPLS-2005 force field in conjunction with the VSGB 2.0 implicit solvation model. Binding free energy (ΔG-bind), expressed in kcal mol^{-1}, was determined using the following equation:

$$\Delta G\text{-bind} = G\text{-complex} - (G\text{-protein} + G\text{-ligand})$$

In this formula, G-complex represents the total energy of the docked complex, incorporating bonded interactions (bond lengths, bond angles, and torsions) as well as non-bonded forces such as van der Waals interactions, electrostatic contributions, hydrogen bonding, and solvation effects. The terms G-protein and G-ligand correspond to the energies of the unbound receptor and ligand, respectively, evaluated independently in their optimized conformations. This method offers a detailed understanding of the binding strength, interaction profile, and thermodynamic favorability of the ligand within the target's active site.[45–47]

3.7.1 Post-dynamic analysis. Following the 100 ns molecular dynamics simulation, the resulting trajectory data were further analyzed using Python-based tools integrated into the Desmond analysis suite (v5.9) to gain in-depth insights into the dynamic properties of the protein–ligand complex. The motion patterns and internal flexibility of the compounds were analysed by Principal Component Analysis (PCA). This statistical method relies on the construction of a covariance matrix of atomic displacements typically for backbone or heavy atoms. The resulting eigenvectors and eigenvalues captured collective motions, and the trajectory was projected along the top principal components to visualize the major conformational transitions occurring throughout the simulation.

In addition, Probability Density Function (PDF) analysis was applied to assess the frequency and distribution of key structural metrics, providing a statistical view of conformational flexibility. For energetic characterization, a Free Energy Landscape (FEL) was generated using the first two principal components. Relative free energy states were derived through the Boltzmann distribution, allowing the identification of low-energy, thermodynamically stable conformations and the transition pathways between them. The post-simulation analyses display a comprehensive view of the complex's conformational heterogeneity, energy stability, and dynamic behavior, enriching our understanding of its potential as a biologically active compound.[48,49]

4 Results and discussion

4.1 Chemistry

The synthetic pathway initiated with commercially sourced (*R*)-carvone **1**, a monoterpene selected as the precursor. Initially, (*R*)-carvone underwent reaction with an equimolar quantity of oxime **2** at 0 °C in the presence of sodium hypochlorite (NaOCl), which acted as the chlorinating reagent, the reaction temperature was carefully controlled to inhibit oxime dimerization. This procedure was subsequently replicated under the same conditions but with an excess of oxime **2**, resulting in the generation of **5**.

It should be noted that the low yield observed for compound **5** can be explained as follows: the first 1,3-dipolar cycloaddition of dipole **2** onto compound **1** occurs at a sterically unhindered vinylic double bond. In contrast, the second addition takes place at a double bond that is highly congested due to its fused position within the carvone ring system. Consequently, the reactivity of this site is significantly diminished, leading to the observed decrease in yield (Fig. 2).

The isoxazoline-carvone intermediates **3a–d** and bis-isoxazoline **5** served as key intermediates for condensation with thiosemicarbazide under acidic catalysis by H_2SO_4. The reactions were carried out in ethanol under reflux for 5 h. This process afforded the target isoxazoline-thiosemicarbazones **4a–d** and bis-isoxazoline-thiosemicarbazone **6** derivatives in satisfactory yields, as depicted in Scheme 1.

In an attempt to improve the low yield of compound **5** (31%), the number of equivalents of dipole **2** was increased. The resulting data are summarized in Table 2.

Table 2 shows the increase in the yield of bis-isoxazoline **5** as the amount of dipole **2** is increased. The yield of **5** improved from 38% to 54% when 3.5 equivalents of **2** were employed. However, increasing the amount to 4 equivalents had no significant impact on the final yield. Consequently, to achieve the highest yield of bis-isoxazoline **5**, it is recommended to conduct the reaction using 3.5 to 4 equivalents of **2**.

The structural elucidation of **4a–d** and **6** was definitively established using HRMS alongside NMR spectroscopy. The HRMS spectra revealed pseudomolecular ion peaks at $m/z = 343.1592$ ($[M + H]^+$) for **4a** and $m/z = 462.1996$ ($[M + H]^+$) for **6**, which closely matched the theoretical molecular formulas $C_{18}H_{22}N_4OS$ and $C_{25}H_{27}N_5O_2S$, respectively, thereby confirming the proposed molecular structures. Analysis of the ^{1}H-NMR spectrum of **6** disclosed two distinctive doublet resonances at 6.67 and 9.19 ppm, corresponding to the NH protons of the thiocarbamoyl moiety (–NH–C(S)═NH). Moreover, two

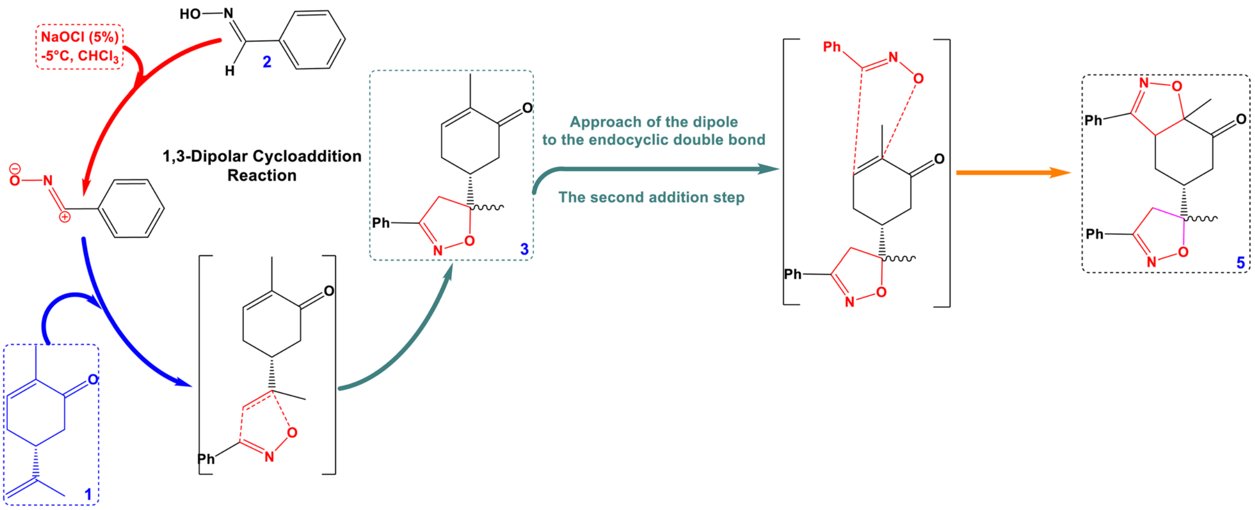

Fig. 2 Synthetic route to mono-isoxazole (**3a–d**) and bis-isoxazole (**5**).

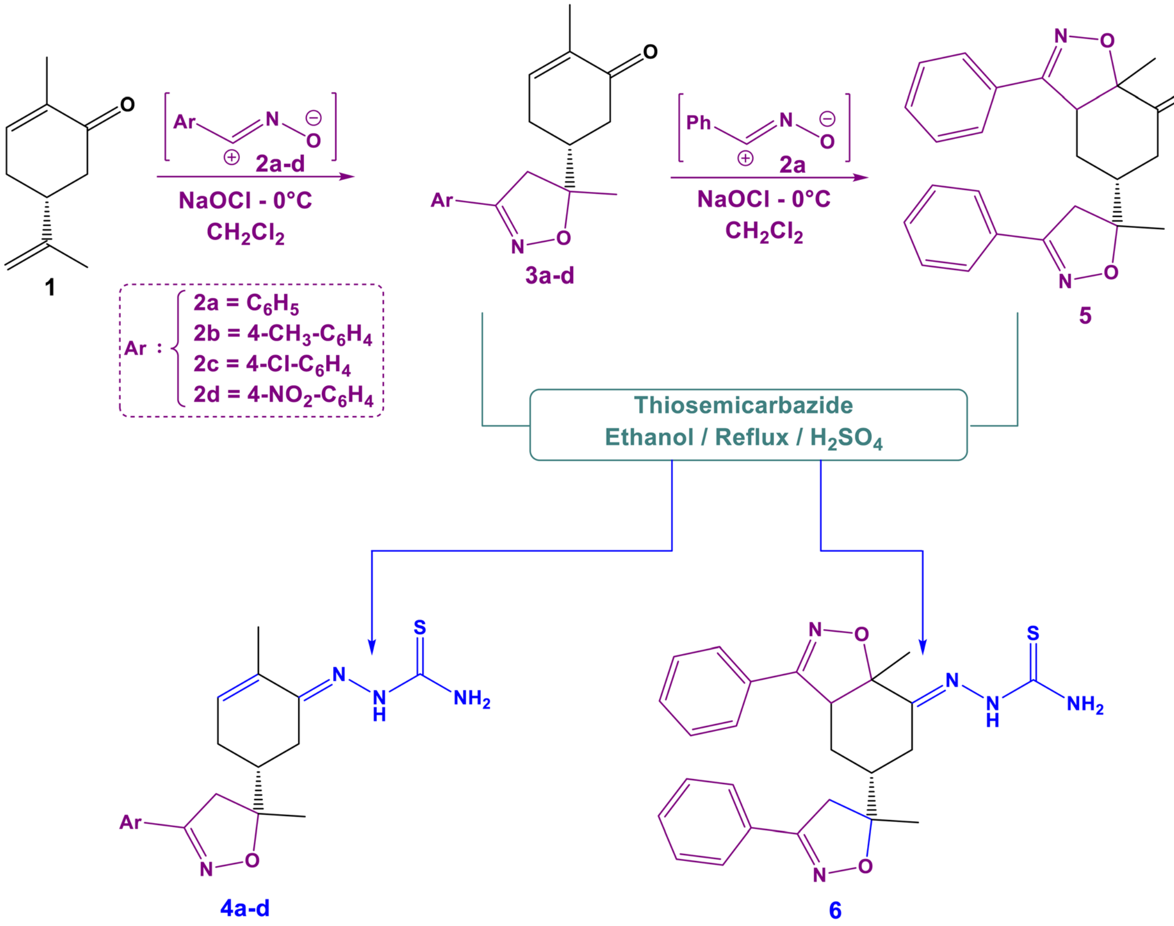

Scheme 1 Stepwise synthesis of mono- and bis-isoxazoline-thiosemicarbazone analogues **4a–d** and **6**.

Table 2 Yield optimization for compound **5**

Equivalent number of 2	2	2.5	3	3.5	4
Yield of compound **5**	31	36	45	51	53

proximate singlet peaks observed at approximately 1.21 and 1.57 ppm were attributed to the methyl groups CH_3 on the carvone hexene ring. Integration of the aromatic proton region accounted for ten protons, consistent with the presence of two aromatic rings within the structure. The ^{13}C-NMR spectra provided conclusive evidence of the condensation reaction between thiosemicarbazide and the carbonyl group of intermediate **5**, as indicated by the absence of the characteristic carbonyl resonance near 205 ppm, which was initially present in compounds **3a** and **5**. In compound **6**, two novel carbon resonances appeared at 179 ppm and 159 ppm, assigned to the thiocarbonyl (C=S) and imine (C=N) carbons, respectively.

4.2 Antibacterial activity

The antibacterial potential of the synthesized compounds **4a–d** and **6** was evaluated against various bacterial strains. These derivatives show promising prospects for applications such as food preservation or as economical complements to existing antibiotic treatments. Overall, the series exhibited moderate antibacterial activity across all tested Gram-negative microorganisms at a concentration of 20 μmoL ml^{-1} (Table 3).

Against *P. aeruginosa*, the new derivatives **4b–d** showed a slight improvement in activity compared to the parent compounds **4a** (9.1 ± 0.10 mm) and **6** (9.5 ± 0.12 mm). Notably, compound **4b** displayed the highest inhibition zone of the series with 11.5 ± 0.10 mm. In contrast, compounds **4c** and **4d** showed more modest activities (8.3 ± 0.6 mm and 9.1 ± 0.9 mm, respectively). While these results indicate a positive trend in the 4-series, these values remain considerably lower than those of Ciprofloxacin (32 ± 0.01 mm) and Co-trimoxazole (31 ± 0.01 mm). Regarding *E. coli*, a similar trend was observed. The new derivative **4b** again proved to be the most potent of the group with an inhibition zone of 13.1 ± 0.74 mm, followed by **4c** (11.8 ± 0.3 mm) and **4d** (11.5 ± 0.5 mm). All three new derivatives outperformed the original compounds **4a** (10.4 ± 0.13 mm) and **6** (9.8 ± 0.12 mm). This suggests that the structural modifications in the **4b–d** sub-series enhance the antibacterial profile against *E. coli*, although they do not yet reach the potency of Ciprofloxacin (37 ± 0.01 mm). The highest sensitivities were recorded against *P. carotovorum*. Compound **4b** exhibited the strongest activity of the entire study with an inhibition zone of 15.4 ± 0.1 mm, slightly surpassing **4a** (14.6 ± 0.12 mm).

Table 3 Zone of inhibition of bacterial growth in mm at the concentration of 20 μmoL ml^{-1} of each product

						Antibiotic			
Product	**4a**	**4b**	**4c**	**4d**	**6**	Ciprofloxacine	Co-trimoxazole	Ampicilline	Bacitracine
Pseudomonas aeruginosa	9.1 ± 0.10	11.5 ± 0.10	8.3 ± 0.6	9.1 ± 0.9	9.5 ± 0.12	32 ± 0.01	31 ± 0.01	0	14 ± 0.05
Escherichia coli	10.4 ± 0.13	13.1 ± 0.74	11.8 ± 0.3	11.5 ± 0.5	9.8 ± 0.12	37 ± 0.01	35 ± 0.01	0	0
Pectobacterium carotovorum	14.6 ± 0.12	15.4 ± 0.1	14.2 ± 0.7	13.6 ± 0.1	9 ± 0.10	45 ± 0.01	37 ± 0.01	0	8 ± 0.08
Staphelococcus	0	0	0	0	0	31 ± 0.01	43 ± 0.01	0	11 ± 0.09

Compounds **4c** (14.2 ± 0.7 mm) and **4d** (13.6 ± 0.1 mm) also demonstrated significant activity, markedly superior to compound **6** (9 ± 0.10 mm). These values are noteworthy, as all derivatives of the 4-series significantly outperformed the antibiotic Bacitracin (8 ± 0.08 mm) against this specific strain, although they remain below Ciprofloxacin (45 ± 0.01 mm). Finally, all tested compounds (**4a–d** and **6**) showed no activity against *Staphylococcus* (0 mm), mirroring the result of Ampicillin (0 mm). This total lack of inhibition, in contrast to the effects of Bacitracin (11 ± 0.09 mm) and Ciprofloxacin (31 ± 0.01 mm), clearly indicates that these derivatives are ineffective against this Gram-positive bacterium under the tested conditions.

The Minimum Inhibitory Concentration (MIC) assessment further confirmed the superior antibacterial potential of the **4a–d** series compared to compound **6**, particularly against Gram-negative strains (Fig. 3). Compounds **4a–d** were highly effective against *Pseudomonas aeruginosa* and *Escherichia coli*, achieving low MIC values ranging from 0.29 to 0.33 μmol mL^{-1}. Specifically, derivative **4c** (bearing the *para*-chloro group) showed the most potent profile against *P. aeruginosa* with an MIC of 0.29 μmol mL^{-1}, while **4b** and **4d** maintained robust activity at 0.312 μmol mL^{-1}. Against *Pectobacterium carotovorum*, the **4a–d** series exhibited even more remarkable efficacy, with MIC values significantly lower than those observed for other strains. Compound **4c** stood out as the most active agent with a remarkably low MIC of 0.14 μmol mL^{-1}, closely followed by **4a** (0.15 μmol mL^{-1}) and **4b** (0.17 μmol mL^{-1}). In comparison, compound **6** demonstrated a much higher MIC of 0.5 μmol mL^{-1} against this same strain, suggesting a lower efficacy and highlighting the structural advantage of the 4-series scaffold in inhibiting *P. carotovorum* growth. In stark contrast, all derivatives (**4a–d** and **6**) demonstrated notably high MIC values of 40 μmol mL^{-1} when tested against *Staphylococcus*. These elevated values signify a lack of significant inhibitory action at therapeutic concentrations against this Gram-positive bacterium. Taken together, these findings reinforce the conclusion that these heterocyclic derivatives are highly selective antibacterial agents, showing potent activity specifically against Gram-negative strains while remaining largely ineffective against Gram-positive organisms.

4.3 Structure–activity relationship (SAR) analysis

The comparative analysis of the antibacterial potency within the **4a–d** series demonstrates that the nature of the *para*-substituent on the aryl moiety significantly modulates the biological activity, following a trend closely linked to electronic and lipophilic properties. Compound **4b**, bearing a *para*-methyl group, consistently emerged as the most potent derivative across all sensitive Gram-negative strains (*P. aeruginosa*, *E. coli*, and *P. carotovorum*), suggesting that the presence of an electron-donating group (+I) increases the electron density of the aromatic system and optimizes interactions with bacterial targets. Furthermore, the slight increase in lipophilicity

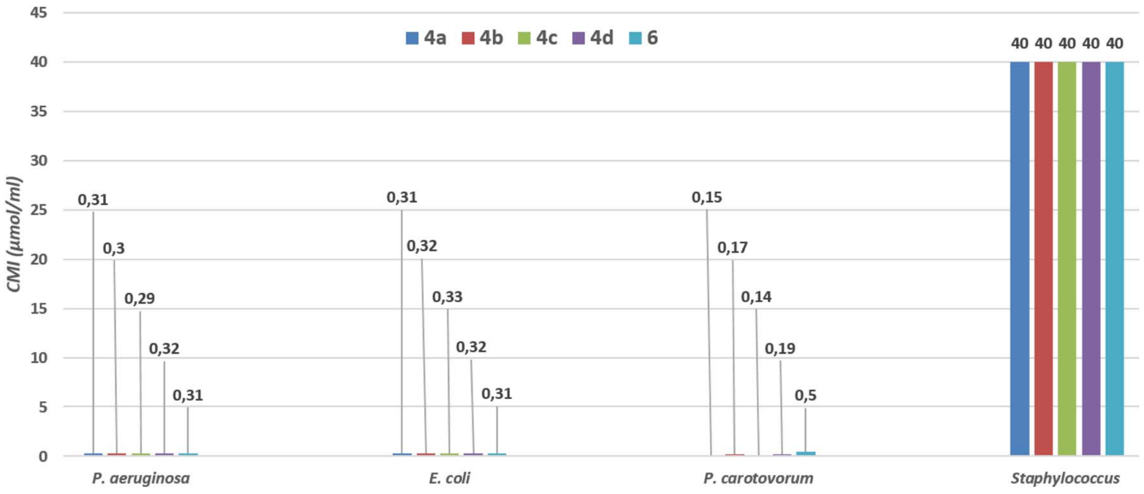

Fig. 3 Minimum inhibitory concentration (MIC) of bacterial growth in μmol ml^{-1}.

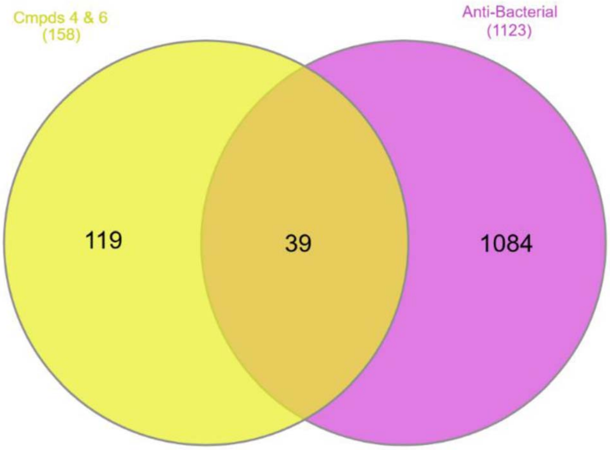

Fig. 4 Disease and designed compound overlapping targets.

provided by the methyl group likely enhances membrane permeability. In contrast, the introduction of electron-withdrawing groups, such as the chlorine atom in **4c** (−I > +M) or the nitro group in **4d** (−I, −M), resulted in a general decrease in activity compared to **4b**, indicating that deactivating the aryl ring is unfavorable for the antibacterial profile of these heterocyclic derivatives. The baseline activity of the unsubstituted compound **4a** (phenyl) confirms that a moderately activating and lipophilic substituent in the *para* position is key to maximizing inhibition zones, leading to an overall SAR trend of CH_3 (**4b**) > H(**4a**) > Cl (**4c**) ≈ NO_2 (**4d**).

4.4 *In silico* studies

4.4.1 Network pharmacology

4.4.1.1. Target identification and overlap analysis. A total of 158 potential target genes associated with the new isoxazole-fused thiosemicarbazide **4a** and **6** scaffolds were identified using the SwissTargetPrediction database. In parallel, 1123 antibacterial (AB)-related genes were retrieved from the GeneCards database. A Venn diagram was then constructed to determine the overlap between **4a** and **6** associated targets and AB-related genes. This analysis yielded 39 common genes, which were considered as key antibacterial targets.

4.4.1.2. Compound-target-pathway network construction. The new molecules, together with the 39 identified key targets and the top antibacterial pathways based on target gene involvement, were integrated into a compound-target-pathway interaction network. This network depicts the interactions between the compounds and multiple targets, thereby highlighting their potential for synergistic therapeutic effects. The multi-target activity of the isoxazole-fused thiosemicarbazide derivatives **4a** and **6** further suggests enhanced efficacy in antibacterial therapy. The overlapping targets within this network are presented in Fig. 4.

4.4.1.3. Protein–protein interaction (PPI) network analysis. All overlapping genes were imported into the STRING database to construct a protein–protein interaction (PPI) network, where each node represents a protein and edges represent functional associations. These interactions reflect the involvement of multiple targets in bacterial pathogenesis and progression. To evaluate the network topology, a network analyser was employed to assess node connectivity, and the resulting PPI data were exported and visualised using Cytoscape software.

The analysis identified key hub genes based on degree centrality, a measure of how many direct connections a node has within the network. Genes with higher degree values are considered more central and potentially more influential in biological processes. The top 10 hub genes identified from the network are listed in Table 4 and visualised in Fig. 5.

The top 10 genes, ranked by degree score, is a measure of their connectivity within a gene interaction network. This highlights the regulators of key biological and disease-related pathways. PTGS2 leads the ranking (degree of 24), highlighting its role in catalysing prostaglandin synthesis during inflammatory responses. AKT1 follows with a degree score of 22; as a central node in cell survival and metabolic signalling, it modulates pathways essential for growth and proliferation. EGFR and CASP3 share the same degree score of 22; EGFR drives mitogenic and oncogenic signalling through receptor tyrosine kinase activity, while CASP3 functions in the initiation of apoptosis, coordinating programmed cell death. MTOR, with a degree of 21, serves as a regulator of cellular growth, nutrient sensing, and autophagy. MMP9 ranks sixth (degree of 19), highlighting its involvement in extracellular matrix remodelling and facilitation of cancer cell invasion. MAPK14 (p38α), with degree of 14, indicating its role in stress-activated signalling cascades that influence inflammation, differentiation, and apoptosis. Finally, PTGS1, CYP3A4, and MAPK8 (JNK1) each exhibit degree scores of 13; PTGS1 maintains baseline prostaglandin production for homeostasis, CYP3A4 stands as a major cytochrome P450 enzyme responsible for xenobiotic metabolism, and MAPK8 transduces stress and cytokine signals, affecting apoptosis and immune responses. The hierarchical ordering of these genes signify their varying degrees of connectivity and functional impact across pathways related to inflammation, cancer, apoptosis, and metabolism.

4.4.1.4. Network pharmacology analysis of top 10 genes. The network pharmacology analysis highlighted the top 10 genes based on their degree of interaction within the constructed protein–protein interaction (PPI) network. The degree score

Table 4 Top 10 genes ranked by degree score

Rank	1	2	3	3	3	3	7	8	8	8
Gene name	PTGS2	AKT1	EGFR	CASP3	MTOR	MMP9	MAPK14	PTGS1	CYP3A4	MAPK8
Degree score	24	22	22	22	21	19	14	13	13	13

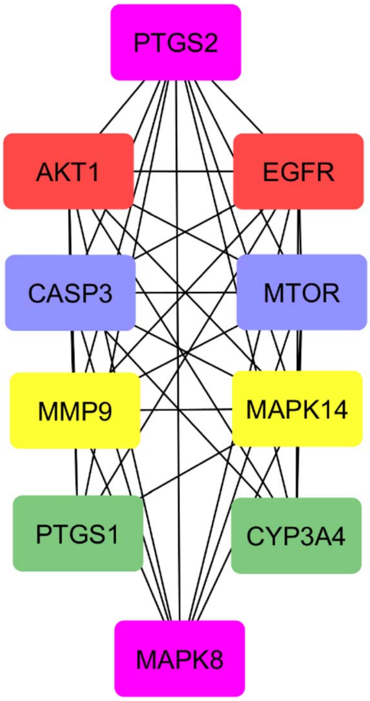

Fig. 5 Top 10 ranked genes network diagram.

reflects the number of direct interactions each gene has with others in the network. These top-ranked genes, along with their corresponding degree scores, are presented in Table 4.

4.4.1.5. Role of top 10 genes in antibacterial activity. PTGS2 and PTGS1 coordinate prostaglandin synthesis to regulate inflammation and maintain epithelial integrity, preventing bacterial translocation across mucosal surfaces. AKT1 signalling supports macrophage and neutrophil survival, enhances phagosome maturation, and promotes reactive oxygen species generation for intracellular bacterial killing. MTOR regulates autophagy, directing intracellular bacteria like Salmonella and Mycobacterium into autophagolysosomes for degradation. EGFR activation in epithelial cells accelerates wound healing and induces secretion of defensins and cathelicidins, establishing antimicrobial barriers. MMP9 facilitates leukocyte infiltration by degrading basement membrane components and can release cryptic antimicrobial peptides from the extracellular matrix. MAPK14 (p38α) amplifies antibacterial defences by driving transcription of cytokines (TNF-α, IL-6, IL-1β) and inducible nitric oxide synthase, enhancing nitric oxide-mediated bacterial killing. MAPK8 (JNK1) activates c-Jun-dependent expression of antimicrobial peptides and mediates apoptosis of infected cells to block bacterial replication. CASP3 executes programmed cell death, ensuring the removal of intracellular niches exploited by pathogens such as Listeria monocytogenes. Finally, CYP3A4 modulates the pharmacokinetics of broad-spectrum antibiotics (*e.g.*, macrolides, fluoroquinolones) and metabolises bioactive lipids that influence immune cell recruitment, thereby indirectly affecting the efficacy and duration of antibacterial therapy. These genes form a synergistic network that balances rapid pathogen eradication with preservation of host tissue function.

The KEGG pathway enrichment analysis and the overview of Biological Processes (BP) in Green, Cellular Components (CC) in Yellow-Green, and Molecular Functions (MF) in Violet are displayed in Fig. 6 and 7, respectively. Based on the KEGG pathway and Gene Ontology (GO) enrichment analyses, PTGS2 (Prostaglandin-Endoperoxide Synthase 2) appears to play a multifaceted role in antibacterial defence mechanisms.

4.4.1.6. KEGG enrichment analysis. PTGS2 is enriched in pathways related to infections and inflammation, including Shigellosis, Human cytomegalovirus infection, and Kaposi sarcoma-associated herpesvirus infection. These associations suggest a potential involvement in host–pathogen interactions and immune responses. Additionally, its role in TNF signaling and Endocrine resistance indicates a function in immune regulation and inflammatory signaling, which are crucial in the bacterial infections.

4.4.1.7. Gene Ontology analysis. In the Biological Process (BP) category, PTGS2 is linked to inflammatory response, signal transduction, oxidative stress, and positive regulation of gene expression. These functions are vital during bacterial invasion, where inflammation and ROS production are part of the defence strategy. Under the Cellular Component (CC), PTGS2 is predominantly associated with the cytoplasm, nucleus, and plasma membrane, highlighting its accessibility and regulatory potential in both signalling and transcriptional regulation during bacterial challenges. In the Molecular Function (MF) domain, enrichment in protein binding, enzyme binding, and ATP binding suggests PTGS2 interacts with various biomolecules to modulate antibacterial defence pathways.

These findings potentiates PTGS2's role in modulating inflammation, immune signaling, and oxidative stress responses that are fundamental to host defense against

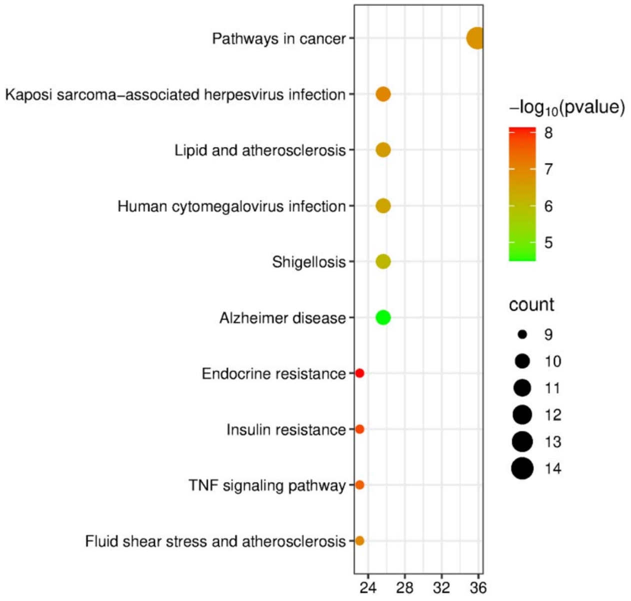

Fig. 6 KEGG enrichment pathways.

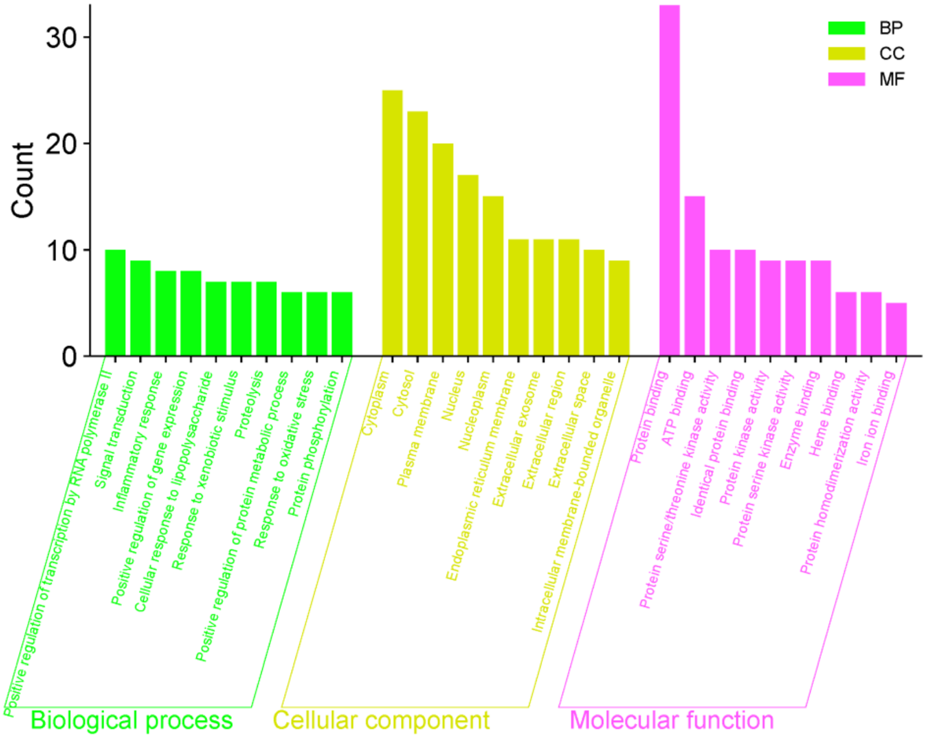

Fig. 7 Overview of biological processes (BP) in green, cellular components (CC) in yellow-green, and molecular functions (MF) in violet.

bacterial pathogens. Its strong involvement in pathogen-related KEGG pathways and immune-regulatory GO terms signifies its potential as a valuable antibacterial target.

4.4.2 Physicochemical properties. The physicochemical properties of the synthesized compounds (**4a–4d** and **6**) indicate that they fall within acceptable ranges for drug-likeness and oral bioavailability when compared with the co-crystal ligand (Table 5). The molecular weights of the compounds range from 342.47 to 461.59 Da, remaining within the preferred limit of <500 Da, suggesting favorable permeability characteristics. The lipophilicity ($\log P$) values lie between 2.34 and 4.81, indicating a balanced hydrophilic–lipophilic profile; compounds **4a**, **4b**, and **4c** show optimal lipophilicity, while compound **6** is relatively more hydrophobic but still within an acceptable range. The topological polar surface area (TPSA) varies significantly, with compounds such as **4d** (149.91 Å^2) showing higher polarity, which may reduce membrane permeability, whereas others like **4a** (72.01 Å^2) and compound **6** (93.61 Å^2) fall within the optimal range (<140 Å^2) for good oral absorption. The number of hydrogen bond acceptors (3–8) and donors (2 for all compounds) complies with Lipinski's criteria, supporting good interaction potential with biological targets. Additionally, the number of rotatable bonds (4–5) suggests moderate molecular flexibility, which is beneficial for binding adaptability without compromising structural rigidity. In comparison, the co-crystal ligand exhibits lower molecular weight and TPSA but higher lipophilicity, indicating stronger hydrophobic character. The synthesized compounds demonstrate favorable physicochemical profiles, with compounds **4a**, **4b**, **4c**, and **6** particularly showing a good balance between lipophilicity, polarity, and flexibility, supporting their potential as drug-like candidates.

4.4.3 ADME studies. The predicted ADME profiles of **4a–d** and **6**, and the co-crystal are presented in Table 6. Demonstrates generally favorable pharmacokinetic characteristics with some distinctions across the series. Most compounds (**4a, 4b, 4c**, and **6**) exhibit high gastrointestinal (GI) absorption,

Table 5 Physicochemical properties of the designed derivatives

Compound	Molecular weight daltons	Log P	TPSA (Å^2)	HBA	HBD	Rot bonds
4a	342.47	3.72	72.01	6	2	4
4b	356.49	3.41	104.09	3	2	4
4c	376.90	3.62	104.09	3	2	4
4d	387.46	2.34	149.91	5	2	5
6	461.59	4.81	93.61	8	2	5
Co-crystal	296.15	5.63	49.33	3	2	3

Table 6 ADME Properties of the designed compounds

Compound	4a	4b	4c	4d	6	Co-crystal
GI absorption	High	High	High	Low	High	High
BBB	No	No	No	No	No	Yes
P-Glyco protein inhibition	Yes	Yes	Yes	Yes	Yes	No
$CaCO_2$ permeability nm s^{-1}	0.87	0.99	0.97	0.77	0.88	1.3
CYP2C9	No	Yes	Yes	Yes	No	No
CYP2D6	Yes	Yes	No	No	Yes	No
CYP3A4	No	Yes	Yes	Yes	No	Yes
PPB %	79.81	83.93	85.10	82.29	89.64	93.82
Log K_p (skin permeation) cm s^{-1}	4	−6.23	−6.17	−6.80	6	6

indicating good potential for oral bioavailability, while compound **4d** shows comparatively lower absorption, possibly due to its higher polarity. None of the synthesized compounds are predicted to cross the blood–brain barrier (BBB), which is advantageous for minimizing central nervous system side effects. The co-crystal ligand is BBB permeable. All synthesized compounds are predicted to be P-glycoprotein (P-gp) inhibitors, suggesting they may enhance intracellular retention but could also influence drug–drug interactions.

The Caco-2 permeability values (0.77–0.99 nm s^{-1}) indicate moderate permeability across intestinal epithelial cells, slightly lower than the co-crystal (1.3 nm s^{-1}), but still within an acceptable range for absorption. Regarding metabolic interactions, compounds **4b**, **4c**, and **4d** show inhibition of CYP2C9 and CYP3A4, while **4a** and **6** do not, suggesting variability in metabolic stability and potential for enzyme-related interactions. For CYP2D6, compounds **4a**, **4b**, and **6** are predicted inhibitors, whereas **4c** and **4d** are not, highlighting compound-specific metabolic profiles.

The plasma protein binding (PPB) values range from ∼79% to 89% for the synthesized compounds, indicating moderate to high binding, which can contribute to sustained systemic circulation while still allowing free drug availability. The co-crystal shows higher PPB (∼93.8%), suggesting comparatively lower free drug fraction. The skin permeation (log K_p) values indicate generally low transdermal permeability for most compounds, although compound **6** shows relatively higher permeability.

The ADME results suggest that the synthesized compounds, particularly **4a–c**, possess a balanced pharmacokinetic profile with good oral absorption, controlled distribution (non-BBB permeable), moderate permeability, and acceptable metabolic characteristics, supporting their suitability for further drug development.

4.4.4 Toxicity studies. Toxicological assessments were performed *in silico* for **4a–d** and **6**, and the co-crystal, evaluating their potential hepatotoxicity, carcinogenicity, immunotoxicity, mutagenicity, and cytotoxicity. The predicted likelihood (probability) for each endpoint is shown in Table 7.

Compounds **4a–4d** are consistently predicted to be non-hepatotoxic (−) with probability values around 0.50–0.51, suggesting a low likelihood of liver-related adverse effects. This is particularly significant when compared to the co-crystal ligand, which shows a positive hepatotoxicity prediction with a higher probability (0.73).

In terms of cytotoxicity, all compounds, including compound **6** and the co-crystal ligand, are predicted to be inactive with probability values ranging from 0.61 to 0.82. This suggests that the compounds are unlikely to cause nonspecific cellular damage. Similarly, the immunotoxicity predictions are favourable for compounds **4a–4d**, all of which are predicted to be inactive with relatively high confidence. This indicates a minimal risk of undesirable immune responses, further supporting their suitability for therapeutic applications.

Regarding mutagenicity, which reflects the potential to cause genetic mutations, compounds **4b** and **4c** are predicted to be non-mutagenic, making them particularly attractive candidates from a genetic safety perspective. Although compounds **4a** and **4d** show positive predictions, the associated probabilities are moderate (0.50 and 0.65, respectively), suggesting that these

Table 7 Toxicity predictions of the synthesised compounds and the cocrystal[a]

	Hepatotoxicity		Carcinogenicity		Immunotoxicity		Mutagenicity		Cytotoxicity	
Compound	Pre^{d}	Pro^{b}	Pre^{dic}	Pro^{b}	Pre^{dic}	Pro^{b}	Pre^{dic}	Pro^{b}	Pre^{dic}	Pro^{b}
4a	(−)	0.50	(+)	0.61	(−)	0.89	(+)	0.50	(−)	0.69
4b	(−)	0.51	(+)	0.58	(−)	0.92	(−)	0.50	(−)	0.69
4c	(−)	0.50	(+)	0.51	(−)	0.61	(−)	0.51	(−)	0.68
4d	(−)	0.51	(+)	0.67	(−)	0.62	(+)	0.65	(−)	0.61
6	(+)	0.51	(+)	0.61	(+)	0.69	(+)	0.55	(−)	0.70
Co-crystal	(+)	0.73	(−)	0.61	(−)	0.99	(−)	0.74	(−)	0.82

[a] (−): inactive; (+): active; Pre^{dic} = prediction; Pro^{b} = probability.

Table 8 Molecular docking results of the synthesised compounds and the cocrystal

Compound	Docking score (kcal mol^{-1})	Number of interacting residues	Number of hydrogen bonds	Number of hydrophobic bonds	Type of interaction
4a	−10.04	10	3	7	Gln461, Gly45, Cys41 (H-bond), Tyr130, Pro153, Val46, Cys47, Pro156, His39 (alkyl), Cys36 (pi-sulphur)
4b	−9.8	12	3	9	Arg44, Tyr130, Gly45 (H-bond), Pro40, Cys47, Cys41, Pro153, Cys36, Pro156, Leu152, Arg469 (Pi-alkyl), Lys137 (unfavorable positive–positive)
4c	−9.5	9	0	9	Pro200, Ala199, Leu390, Leu391, (Pi–Pi T shaped), Ala202, Trp387, Tyr385 (pi-alkyl), His207, His386 (Pi-cation)
4d	−8.32	9	4	5	Arg469, Arg44, Gln461, Pro154 (H-bond), Pro153, Pro156, His39, Cys47, Cys36 (pi-alkyl)
6	−9.95	4	0	4	Ala202, Val295, Val447 (alkyl), Leu391 (pi-sigma)
Co-crystal	−7.81	10	2	8	Ser530, Tyr385 (H-bond), Phe518, Leu352, Val523, Leu531, Ala527 (alkyl), Val349 (pi-sigma), Met522 (pi-sulphur), Gly526 (amide-pi stacked)

risks are not definitive and may be mitigated through structural optimization. The co-crystal ligand is predicted to be non-mutagenic.

All synthesized compounds (**4a–4d**) display a positive result for carcinogenicity, with probability values ranging from 0.51 to 0.67. However, these probabilities are moderate and do not indicate a high carcinogenic risk. They require experimental confirmation. Importantly, compound **6** shows comparatively higher predicted activity across multiple toxicity endpoints, including hepatotoxicity, immunotoxicity, and mutagenicity, suggesting that it may have less favourable safety.

The toxicity analysis highlights that the majority of the synthesized compounds, exhibit a balanced and favourable safety profile, characterized by low hepatotoxicity, absence of cytotoxicity, minimal immunotoxic risk, and no mutagenic potential. These findings support the potential of the

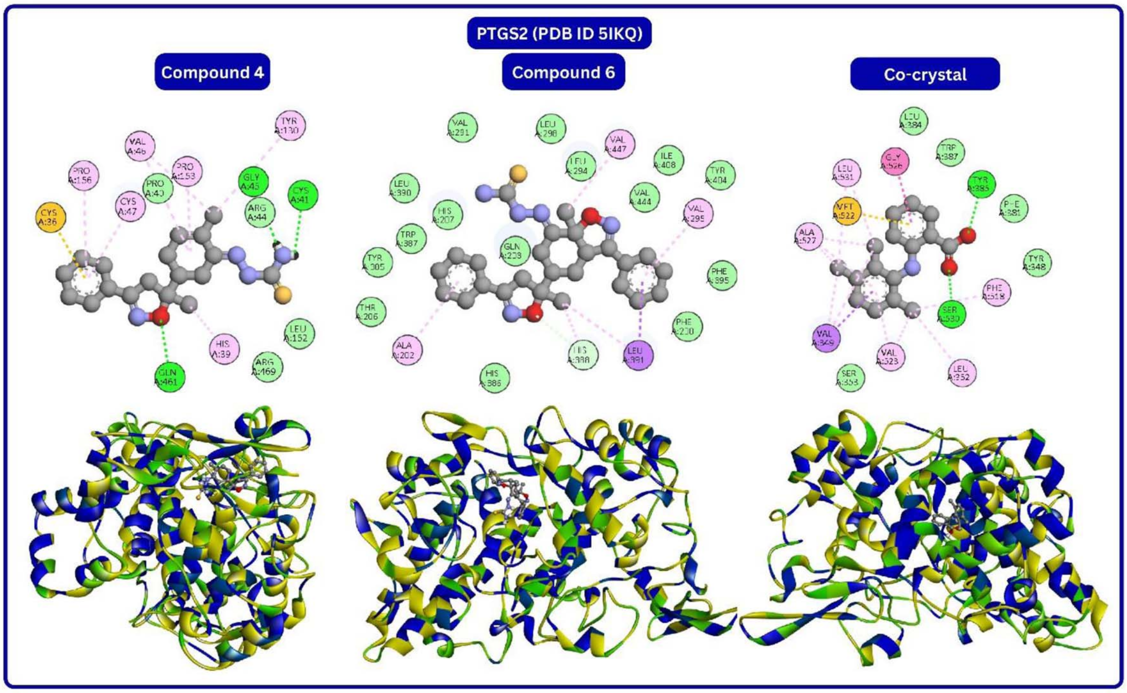

Fig. 8 2D/3D representation of the synthesised compounds and the co-crystal.

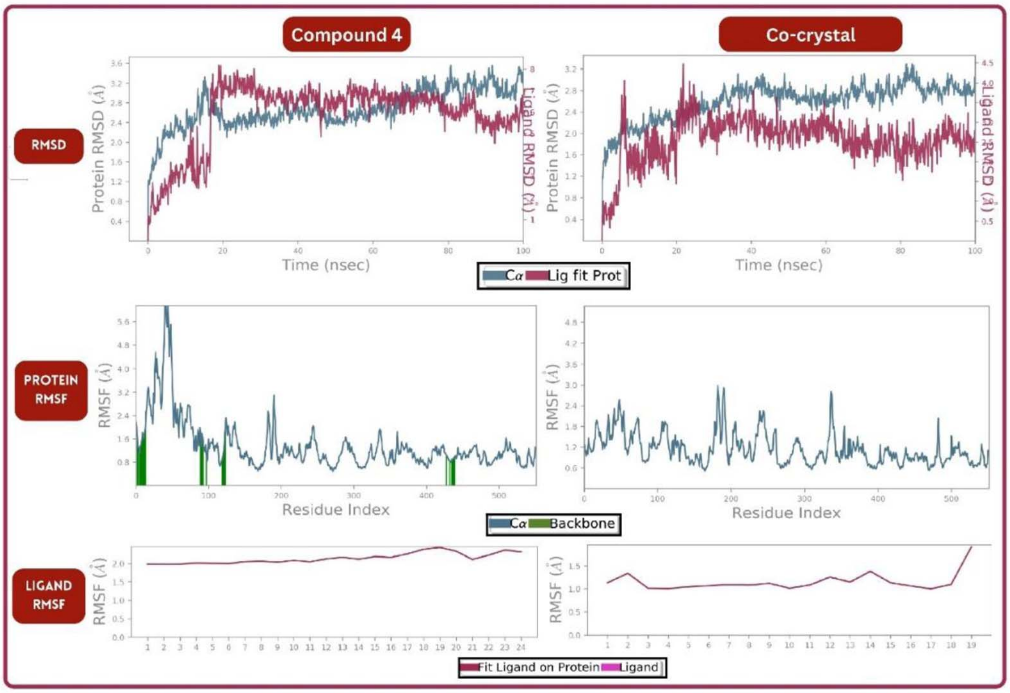

Fig. 9 RMSD, protein RMSF and ligand RMSF plots of the compound **4a** and the cocrystal.

synthesized compounds as safe and viable for further optimization and biological evaluation.

4.4.5 Molecular docking. The molecular docking results of **4a** and **6** demonstrated promising binding affinities toward the target protein, as summarized in Table 8. The corresponding 2D and 3D interaction diagrams of the docked complexes, alongside the reference cocrystal structure, are presented in Fig. 8. The docking results demonstrate that both **4a** and **6** exhibit stronger binding affinities to the target protein compared to the co-crystallised ligand. Compound **4a** achieved the most favourable docking score of −10.04 kcal mol^{-1}, indicating a highly stable and energetically favourable interaction. Compound **6** also showed a good docking score of −9.95 kcal mol^{-1}, while the co-crystal ligand had a comparatively weaker binding score of −7.81 kcal mol^{-1}. These values suggest that both synthesised compounds bind more effectively than the reference ligand within the active site of the protein.

Compound **4a** exhibited a rich interaction profile involving 10 interacting residues. It formed three hydrogen bonds with residues Gln461, Gly45, and Cys41, which are key contributors to binding specificity and stability. It established seven hydrophobic interactions, including alkyl bonds with residues such as Tyr130, Pro153, and His39, and a π-sulphur interaction with Cys36. This diverse range of interactions reflects a strong and stable association with the target site.

Compound **4b** showing the binding affinity (−9.8 kcal mol^{-1}), followed by **4c** (−9.5 kcal mol^{-1}) and **4d** (−8.32 kcal mol^{-1}). Compound **4b** forms three hydrogen bonds with key residues such as Arg44, Tyr130, and Gly45, which significantly contribute to binding specificity and stability. Additionally, it engages in multiple hydrophobic interactions with residues including Pro40, Cys47, Cys41, and Leu152, along with a π-alkyl interaction with Arg469. However, the presence of an unfavorable positive–positive interaction with Lys137 may slightly reduce its overall binding efficiency despite the strong score.

Compound **4c**, although slightly lower in binding energy, demonstrates a hydrophobic-dominated interaction profile with no hydrogen bonds but strong π–π T-shaped interaction with aromatic residues (such as Trp387 and Tyr385) and π-cation interactions involving His207 and His386. These interactions help stabilize the ligand within the binding pocket through non-polar and aromatic stacking interactions, compensating for the absence of hydrogen bonds.

Compound **4d** shows a comparatively weaker binding affinity and forms four hydrogen bonds with residues such as Arg469, Arg44, Gln461, and Pro154, indicating good polar interactions. However, its overall interaction network is less extensive, with fewer hydrophobic contacts and moderate π-alkyl interactions involving residues like Cys47 and Cys36.

Compound **6**, showed a simpler interaction pattern, involving only four residues, all through hydrophobic interactions. These included alkyl bonds with Ala202, Val295, and Val447, and a π-sigma interaction with Leu391. Importantly, no hydrogen bonds were detected for compound **6**, which could slightly affect its binding stability despite a good docking score. The absence of polar interactions may suggest that its binding relies mainly on hydrophobic complementarity.

The co-crystallised ligand, used as a reference, interacted with 10 residues, forming two hydrogen bonds with Ser530 and Tyr385, and eight hydrophobic interactions. It formed specialised contacts like π-sulphur (Met522) and amide-π stacking

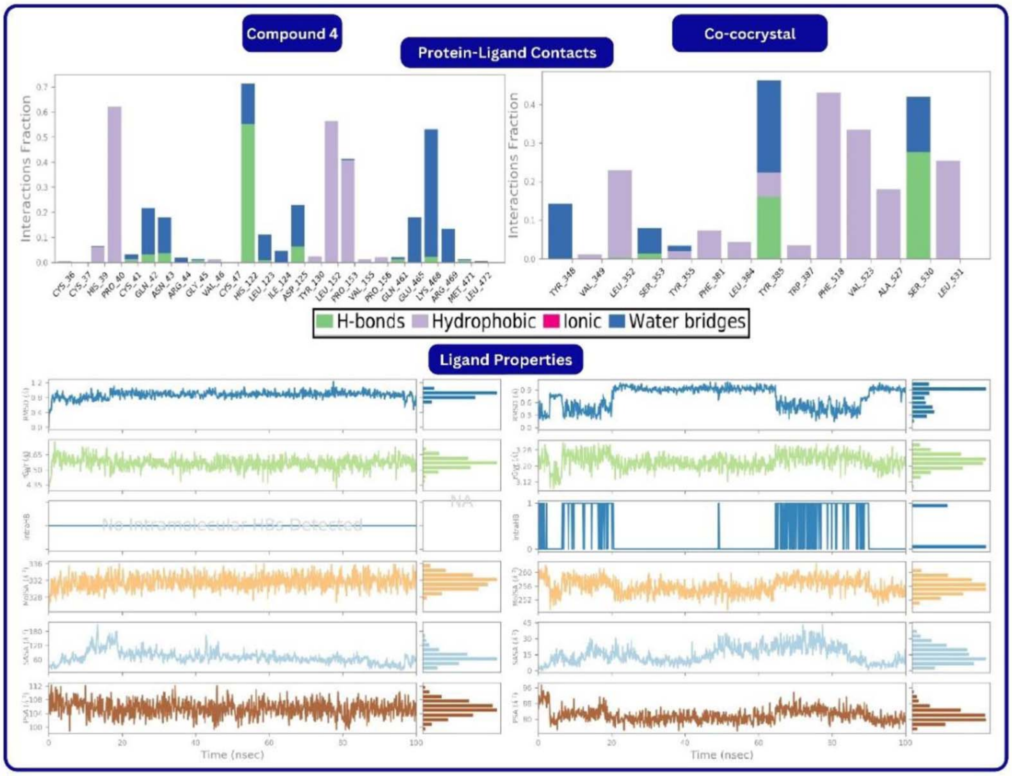

Fig. 10 Protein–ligand contacts and the ligand properties of the **4a** and the cocrystal.

(Gly526). While this interaction profile is balanced, the overall binding energy is weaker than those of the synthesised compounds.

These findings indicate that compound **4a** exhibits the most favorable binding profile, characterized by strong binding energy and a diverse set of molecular interactions. Compound **6** also displayed considerable potential. However, its lack of hydrogen bonding interactions suggests that further structural optimization may be required. Overall, the superior docking performance of both compounds, relative to the co-crystallized ligand, highlights their potential as promising antibacterial candidates.

4.4.6 Molecular dynamics. A 100-nanosecond molecular dynamics (MD) simulation was carried out to evaluate the conformational dynamics and structural stability of **4a** in complex with PTGS2. The simulation encompassed several key analyses, including Root Mean Square Deviation (RMSD), Root Mean Square Fluctuation (RMSF), protein–ligand interaction profiling, and assessment of ligand-specific properties, thereby providing a comprehensive understanding of the complex's behavior throughout the simulation period.

4.4.6.1. RMSD. The RMSD plots (Fig. 9) provided insights into the overall stability of the protein–ligand complexes during the simulation. For the compound **4**-PTGS2 complex, the protein RMSD started at approximately 1.2 Å and gradually increased to around 3.2 Å within the first 20 ns. Following this initial rise, the RMSD showed a mild fluctuation, stabilizing between 2.4 and 3.2 Å for the remainder of the simulation, suggesting that the protein maintained structural integrity with moderate flexibility. The ligand RMSD for **4a** began at 1.0 Å and increased steadily to around 4.0 Å by 20 ns. It peaked at approximately 7.0 Å at 30 ns, indicating conformational rearrangements in the ligand. After this point, the RMSD showed slight fluctuations, remaining between 6.0 and 7.0 Å until 90 ns, and finally reduced to 5.0–6.0 Å by the end of the simulation. These observations suggest that while the ligand underwent significant movement within the binding pocket, it remained engaged with the protein.

The co-crystal-PTGS2 complex exhibited a protein RMSD that started at 1.6 Å, gradually increased to 2.4 Å by 20 ns, and reached a maximum of 2.8 Å around 40 ns. For the remaining simulation period, the RMSD fluctuated slightly within the range of 2.4–2.8 Å, reflecting a relatively stable protein conformation. The ligand RMSF initially rises from 0.5 Å to 4.0 Å within the first 10 ns, then decreases to a range of 1.5–2.5 Å by 20 ns. It subsequently increases again to 4.0 Å and fluctuates between 2.5–3.2 Å up to 60 ns. In the final phase of the simulation, the RMSF stabilizes within the range of 2.0–3.0 Å and remains consistent until 100 ns.

4.4.6.2. RMSF. The Root Mean Square Fluctuation (RMSF) analysis was conducted to evaluate the flexibility of individual amino acid residues and ligand atoms throughout the simulation period (Fig. 9). For the compound **4a**-PTGS2 complex, the protein RMSF values were predominantly below 1.6 Å, indicating limited fluctuations and suggesting that most residues remained relatively stable. The ligand RMSF values were

Table 9 Average binding free energy calculations of the **4a** and the cocrystal

Compound	ΔG bind free energy (kcal mol^{-1})	ΔG bind coulomb (kcal mol^{-1})	ΔG bind covalent (kcal mol^{-1})	ΔG bind VdW (kcal mol^{-1})	ΔG bind H-bond (kcal mol^{-1})	ΔG bind lipophilic (kcal mol^{-1})
4a	−74.98	−20.09	−4.93	−49.92	−1.95	−30.09
Co-crystal	−74.98	−19.87	−5.07	−50.16	−1.97	−30.15

generally under 2.0 Å, reflecting moderate flexibility of the ligand atoms within the binding site. The co-crystal-PTGS2 complex showed slightly higher protein RMSF values, mostly below 1.8 Å, while the ligand RMSF values were slightly lower, staying under 1.5 Å. This suggests that although the protein exhibited marginally greater flexibility, the co-crystal ligand maintained a more rigid conformation during the simulation.

4.4.6.3. Protein–ligand contacts. Protein–ligand interaction provided insights into the stabilizing interactions formed between the ligands and PTGS2, highlighting both the nature and duration of key contacts throughout the simulation (Fig. 10). In the compound **4**-PTGS2 complex, His122 exhibited a strong hydrogen bonding interaction with a fraction of up to 0.6 Å, and also participated in a water bridge interaction reaching an interaction fraction of 0.7 Å. Pro40, Leu152, and Pro153 were involved in stable hydrophobic interactions, each showing fractions of up to 0.6 Å. Additionally, Lys468, Gln42, Asn43, and Asp125 contributed to hydrogen bonding, though with relatively lower interaction fractions, indicating transient or weaker contacts.

In the co-crystal-PTGS2 complex, Tyr385 formed a weak hydrogen bond with an interaction fraction of 0.4 Å, accompanied by hydrophobic interactions and a water bridge of similar fraction. Ser530 displayed a strong and stable hydrogen bond (interaction fraction up to 0.3 Å) along with a water bridge interaction up to 0.4 Å, indicating a significant role in ligand stabilization. Phe518 and Val523 were engaged in hydrophobic interactions with interaction fractions up to 0.4 and 0.3 Å, respectively. Ser353 also formed a weak hydrogen bond, contributing to the overall binding stability of the complex.

4.4.6.4. Ligand properties. Ligand-specific properties, including radius of gyration (rGyr), molecular surface area (MolSA), solvent-accessible surface area (SASA), and polar surface area (PSA), were monitored throughout the 100-nanosecond MD simulation to assess the compactness, exposure, and polarity of the ligands (Fig. 10).

For compound **4a**, the radius of gyration (rGyr) began at approximately 4.35 Å and gradually increased to stabilise within the range of 4.50 to 4.65 Å, maintaining this conformation for the remaining time of the simulation, indicating consistent molecular compactness. The MolSA values remained stable between 328 and 332 Å^2, showing minimal fluctuations and suggesting a relatively constant molecular surface throughout the simulation. The SASA initially measured around 60 Å^2, peaked at 180 Å^2 around the 20 ns, and then declined to a stable range between 60 and 120 Å^2 till the end of the simulation, indicating changes in solvent exposure. The PSA started between 104 and 108 Å^2 during the first 20 ns, followed by a slight reduction and stabilisation within 100 to 104 Å^2, reflecting a moderate change in polar exposure.

In comparison, the co-crystal ligand exhibited a rGyr value that oscillated between 3.20 and 3.28 Å during the first 20 ns, decreased to 3.20 Å by 60 ns, and then returned to the earlier range up to 100 ns, reflecting a more compact and slightly flexible structure. The MolSA started at 260 Å^2 and remained within 256 to 260 Å^2 during the early simulation period. Then it dropped slightly to 252–256 Å^2 by 60 ns, and returned to 256–

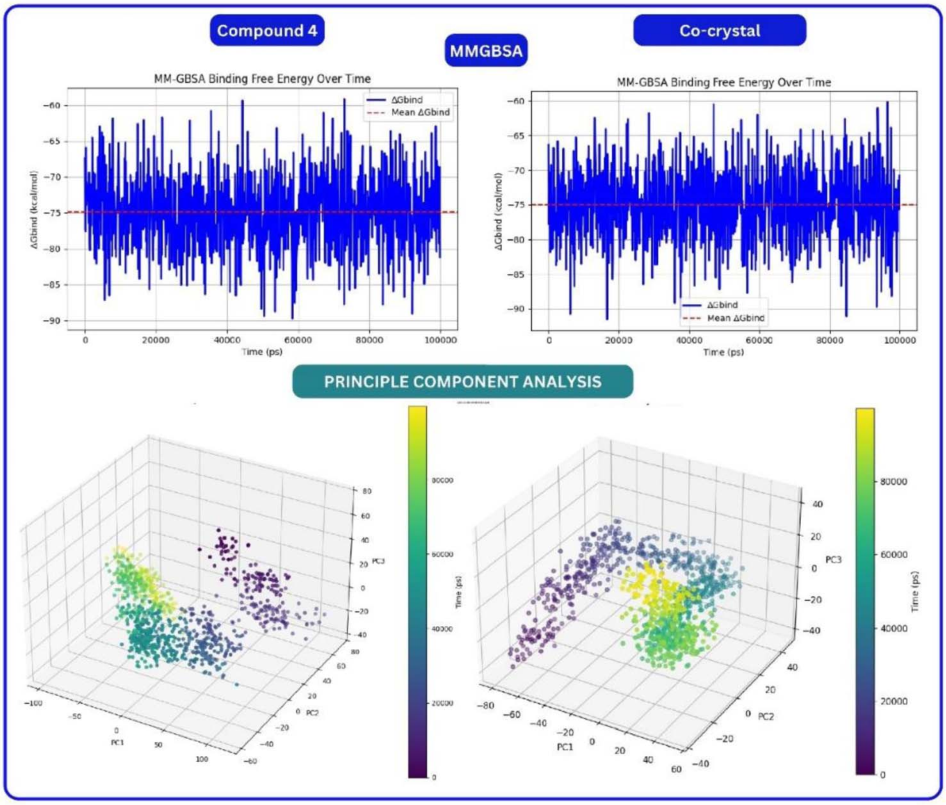

Fig. 11 MMGBSA and PCA plots of the **4a** and the cocrystal.

260 Å^2 by the end, indicating mild fluctuations in molecular size. The SASA began at nearly 0 Å^2 and remained under 15 Å^2 for the first 10 ns. It then increased to 15–30 Å^2 until 30 ns, decreased again below 15 Å^2 up to 50 ns, and fluctuated between 15 and 30 Å^2 until 80 ns before returning to 0–15 Å^2, reflecting transient solvent exposure. The PSA initially ranged from 88 to 96 Å^2, gradually declined to around 80 Å^2, and remained relatively stable until 60 ns, followed by a slight increase to 80–88 Å^2 until 100 ns.

The comparative analysis of the compound **4**-PTGS2 and co-crystal-PTGS2 complexes revealed that compound **4a** induced greater ligand mobility and transient fluctuations in solvent exposure, yet maintained stable protein conformation and compactness. Despite exhibiting higher ligand RMSD and moderate flexibility, compound **4a** consistently interacted with key PTGS2 residues through strong hydrogen bonding and hydrophobic contacts, indicating sustained binding. In contrast, the co-crystal ligand demonstrated a more compact and rigid profile with limited solvent exposure, suggesting a tighter but less dynamic fit. These outcomes suggest, compound **4a** possesses adaptive binding behaviour, preserving crucial protein–ligand interactions while allowing conformational flexibility, highlighting its potential as a PTGS2-targeting antibacterial candidate.

4.4.7 MM-GBSA analysis. The Molecular Mechanics Generalized Born Surface Area (MM-GBSA) results provide a detailed breakdown of the energetic contributions that govern the binding affinity of the compound PTGS2-**4a** complex, and compared against the co-crystal ligand. The results are presented in Table 9 and Fig. 11.

Both compound **4a** and the co-crystal exhibit total binding free energy (Δ*G*-bind) of −74.98 kcal mol^{-1}, suggesting that their overall binding affinities to PTGS2 are comparable. However, the individual energy components reveal subtle differences in stabilising the protein–ligand complex. The van der Waals (Δ*G*-bind VdW) contribution is slightly more favourable for the co-crystal (−50.16 kcal mol^{-1}) compared to **4a** (−49.92 kcal mol^{-1}), indicating a marginally stronger non-polar interaction between the co-crystal and the PTGS2 binding site. Similarly, hydrogen bonding (Δ*G*-bind H-bond) and covalent interaction energies are slightly more negative for the co-crystal (−1.97 and −5.07 kcal mol^{-1}, respectively) than for **4a** (−1.95 and −4.93 kcal mol^{-1}), suggesting that the co-crystal may form more optimal or stable hydrogen bonds and covalent-like interactions within the binding pocket. On the other hand, coulombic interactions (Δ*G*-bind Coulomb) are slightly more favorable for **4a** (−20.09 kcal mol^{-1}) than for the co-crystal (−19.87 kcal mol^{-1}), indicating a stronger electrostatic interaction between **4a** and PTGS2. The lipophilic contribution (Δ*G*-bind Lipophilic) of **4a** and standard are similar in range (−30 kcal mol^{-1}). This suggests that compound **4a** experiences favorable lipophilic interactions that similar to standard enhance its overall binding stability. These results reveal that compound **4a** benefits from a more favorable lipophilic interaction profile and better electrostatics, potentially making it a more pharmacodynamically robust ligand compared to the co-crystal.

4.4.7.1. Principal component analysis (PCA) of molecular dynamics trajectories. Principal Component Analysis (PCA) was conducted to investigate and compare the conformational dynamics of the compound PTGS2-**4a** complex and the co-crystal-PTGS2 complex over a 100 ns molecular dynamics (MD) simulation (Fig. 11). For the compound PTGS2-**4a** complex, the trajectory initially exhibited scattered movements within the positive regions of both PC1 and PC2. As the simulation progressed, particularly by around 40 ns, the complex transitioned toward the central region of the principal component space and began to drift into the negative region of PC3. From 40 to 60 ns, a stable conformational cluster emerged in the negative region of PC1, followed by a gradual shift toward a second cluster located further along the negative PC1 axis, which persisted until the end of the 100 ns simulation. This progression suggests a transition between two dominant conformational states during the simulation period. The co-crystal-PTGS2 complex displayed a different pattern of conformational movement. Initially, the complex showed scattered dynamics within the PC2 range of −40 to +40, while remaining in the negative region of PC1 during the first 20 ns. Between 20 and 40 ns, the system moved toward the positive side of PC1, reflecting a shift in dominant motion. After this transition, the complex gradually settled toward the centre of the PCA space, eventually forming a single stable conformational cluster that persisted until the end of the 100 ns simulation. PCA revealed that while both complexes undergo conformational transitions, compound **4a** displayed a more dynamic behavior with distinct state transitions, whereas the co-crystal complex stabilized earlier, suggesting relatively less structural fluctuation over time.

4.4.7.2. Probability density function (PDF) analysis. The Probability Density Function (PDF) analysis of the principal components (PC1 and PC2), obtained from the molecular dynamics simulation trajectories, explains the conformational stability and dominant structural states of the protein–ligand complexes (Fig. 12). For the compound **4a**-PTGS2 complex, the PDF plot of PC1 reveals a broad distribution spanning from −100 to +100 along the PC1 axis. This wide spread indicates greater conformational flexibility, with relatively mild density peaks around 0.005, suggesting the absence of a single dominant conformational state. The PC2 exhibits a more defined distribution within the −50 to +50 range, with two distinct

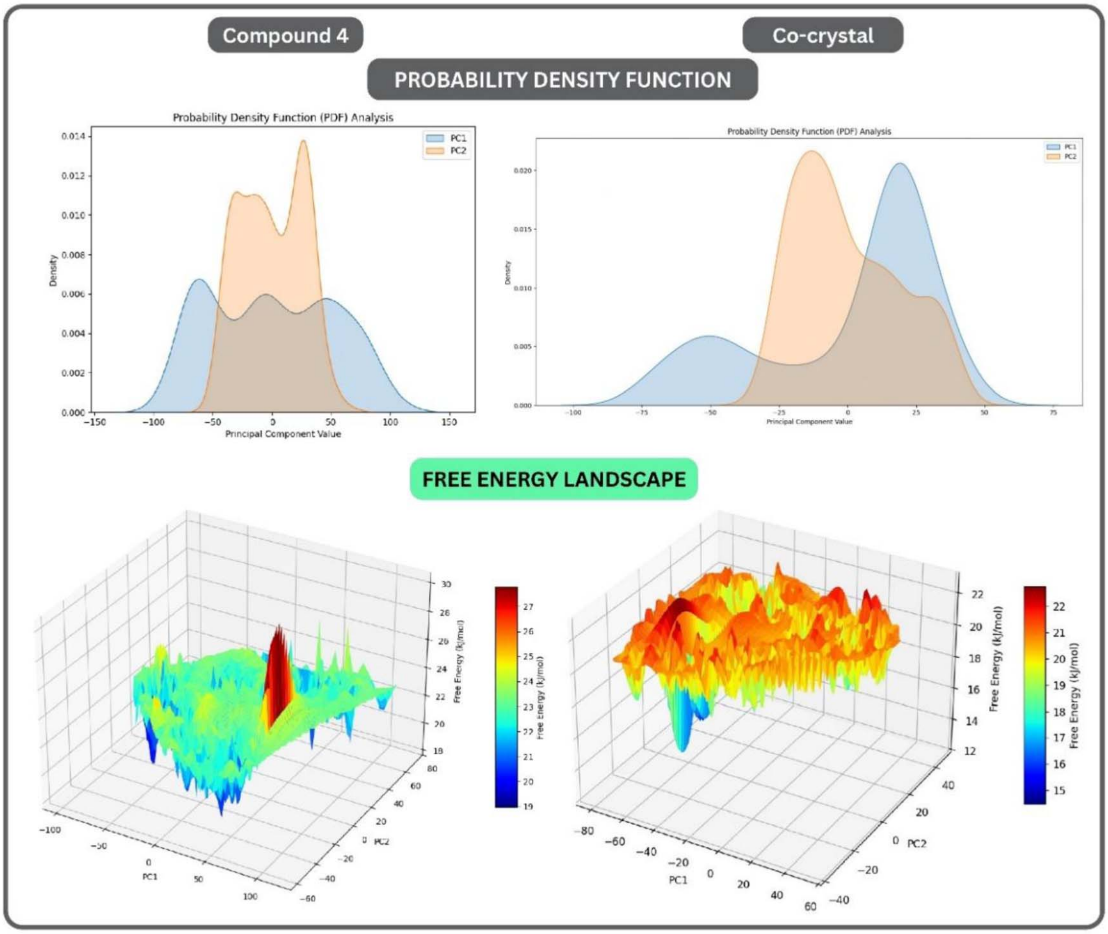

Fig. 12 PDF and FEL plots for the **4a** and the cocrystal.

peaks observed at densities of 0.011 and 0.014. These peaks point to two moderately preferred structural states along this component.

For the co-crystal-PTGS2 complex, the PDF of PC1 displays two blunt peaks located at approximately −50 and +25, with corresponding density values of 0.005 and 0.020, respectively. This bimodal distribution suggests the existence of two preferred conformations. The PDF of PC2 shows a broader range extending up to +40, with a prominent peak at −20 and a maximum density of 0.020, indicating a relatively stable and dominant structural state along this component. From these findings, compound **4a** exhibits broader conformational sampling and defined conformational preferences compared to the cocrystal, reflecting greater stability during the simulation.

4.4.7.3. Free energy landscape (FEL) analysis. The Free Energy Landscape (FEL) analysis offers a visual representation of the conformational diversity and thermodynamic stability of protein–ligand complexes over the course of molecular dynamics simulations. Constructed using the first two principal components (PC1 and PC2) derived from PCA, the FEL plot highlights regions of low and high free energy, reflecting stable and unstable structural states, respectively. In this plot, deep blue areas correspond to low-energy, highly stable conformations, while green, yellow, and red regions represent progressively higher energy and less stable or transient states (Fig. 12).

For the compound PTGS2-**4a** complex, the FEL plot reveals multiple deep blue basins, indicating stable conformational states. These basins are distributed across a range of −100 to +50 along PC1 and −20 to +80 along PC2, with corresponding energy values between 19 and 21 kJ mol^{-1}. These regions are surrounded by blue to green zones, representing moderately stable conformations with energy values ranging from 21 to 24 kJ mol^{-1}. The area from 0 to +50 along PC1 displays clustered high-energy peaks, shown in yellow to red, corresponding to free energy values of 25 to 27 kJ mol^{-1}. These peaks indicate less favorable and more transient conformations.

The FEL plot of the co-crystal-PTGS2 complex features a broad and moderately rugged energy surface. The most stable conformational states are visualized as deep blue and cyan basins located predominantly within the −80 to −40 range of PC1 and extending toward neutral to slightly negative values along PC2. These low-energy basins represent free energy values in the range of 12–15 kJ mol^{-1}, signifying high structural stability. Surrounding these areas, the landscape transitions to yellow and orange regions, with energy values between 18 and 21 kJ mol^{-1}, suggesting moderately stable conformations frequently visited during the simulation. Additionally, scattered red patches, especially between −20 to +40 along PC1 and 0 to +40 along PC2, indicate high-energy conformations reaching up to 22–23 kJ mol^{-1}, which are likely associated with unstable or short-lived states of the complex. These outcomes of the FEL plot state that compound **4a** exhibits broader energy fluctuations and more low-energy transitions, whereas the co-crystal complex demonstrates deeper and more concentrated high-energy minima. This low-energy conformational preference by the compound **4a** indicates greater conformational stability within the binding pocket.

5 Conclusion

In the present study, novel thiosemicarbazone derivatives were synthesized and thoroughly characterized by ^{1}H- and ^{13}C-NMR spectroscopy as well as mass spectrometry. The obtained spectroscopic data confirmed the successful synthesis of these compounds in high yields. The antibacterial activity of the derivatives was evaluated *in vitro* against both Gram-positive and Gram-negative bacterial strains using the well diffusion method. Compounds **4a–d** and **6** exhibited notable antibacterial potency, with minimum inhibitory concentration (MIC) values ranging from 0.31 to 0.5 μg mL^{-1}. Following these antibacterial results, *in silico* studies were performed on compounds **4a–d** and **6**, which consistently demonstrated stable binding interactions with key residues within the active site (PTGS2). Molecular dynamics simulations of PTGS2-**4a** complexes further indicated substantial structural stability throughout the simulation period. Additionally, the MM-GBSA, PCA, PDF, and FEL analyses consistently highlight compound **4a**'s superior or comparable performance relative to the reference inhibitor, Resatorvid. Specifically, MM-GBSA calculations revealed slightly more favorable binding free energy for **4a**. PCA and PDF analyses indicated its more rapid and stable conformational stabilization, and FEL analysis demonstrated a more dominant and energetically favorable binding landscape. These promising findings warrant further investigation, including the synthesis of metal complexes derived from the selected compounds and their subsequent *in vivo* evaluation as antimicrobial, antiviral, and anticancer agents in future studies.

Author contributions

Mubarak A. Alamri, Yassine Riadi, Ali Altharawi, Taibah Aldakhil: biological activity, study design, investigation, preparation, writing – original draft; Reda A. Haggam and Bharath Kumar Chagaleti: writing – original draft and *in silico* study; Ait Itto Moulay Youssef and Ali Oubella: writing – original draft, study design, investigation, characterization. All authors reviewed the manuscript.

Conflicts of interest

The authors have no relevant affiliations or financial involvement with any organization or entity with a financial interest in or financial conflict with the subject matter or materials discussed in the manuscript. This includes employment, consultancies, honoraria, stock ownership or options, expert testimony, grants or patents received or pending, or royalties.

Data availability

All the data analysed during the current study are available in the manuscript.

Supplementary information: spectral data. See DOI: https://doi.org/10.1039/d5ra09902a.

Acknowledgements

The authors extend their appreciation to Prince Sattam bin Abdulaziz University for funding this research work through the project number (PSAU/2025/03/36922).

References

1 J. R. Rohr, C. B. Barrett, D. J. Civitello, M. E. Craft, B. Delius, G. A. DeLeo, P. J. Hudson, N. Jouanard, K. H. Nguyen, R. S. Ostfeld and J. V. Remais, Emerging human infectious diseases and the links to global food production, *Nat. Sustain.*, 2019, **2**(6), 445–456, DOI: 10.1038/s41893-019-0293-3.

2 Z. Breijyeh, B. Jubeh and R. Karaman, Resistance of gram-negative bacteria to current antibacterial agents and approaches to resolve it, *Molecules*, 2020, **25**(6), 1340, DOI: 10.3390/molecules25061340.

3 T. Tängdén, E. Carrara, M. M. Hellou, D. Yahav and M. Paul, Introducing new antibiotics for multidrug-resistant bacteria: obstacles and the way forward, *Clin. Microbiol. Infection*, 2025, **31**(3), 354–359, DOI: 10.1016/j.cmi.2024.09.025.

4 H. Sati, E. Carrara, A. Savoldi, P. Hansen, J. Garlasco, E. Campagnaro, S. Boccia, J. A. Castillo-Polo, E. Magrini, P. Garcia-Vello and E. Wool, The WHO Bacterial Priority Pathogens List 2024: a prioritisation study to guide research, development, and public health strategies against antimicrobial resistance, *Lancet Infect. Dis.*, 2025, **25**(9), 1033–1043, DOI: 10.1016/S1473-3099(25)00118-5.

5 S. F. Feldman, E. Temkin, L. Wullfhart, A. Nutman, V. Schechner, P. Shitrit, R. Shvartz, M. J. Schwaber, A. Andremont and Y. Carmeli, A nationwide population-based study of Escherichia coli bloodstream infections: incidence, antimicrobial resistance and mortality, *Clin. Microbiol. Infection*, 2022, **28**(6), 879, DOI: 10.1016/j.cmi.2021.12.009.

6 R. H. Abd El-Aleam, R. F. George, H. H. Georgey and H. M. Abdel-Rahman, Bacterial virulence factors: a target for heterocyclic compounds to combat bacterial resistance, *RSC Adv.*, 2021, **11**(58), 36459–36482, DOI: 10.1039/D1RA06238G.

7 M. Aatif, M. A. Raza, K. Javed, S. M. Nashre-ul-Islam, M. Farhan and M. W. Alam, Potential nitrogen-based heterocyclic compounds for treating infectious diseases: a literature review, *Antibiotics*, 2022, **11**(12), 1750, DOI: 10.3390/antibiotics11121750.

8 S. Yuan, D. D. Shen, Y. R. Bai, M. Zhang, T. Zhou, C. Sun, L. Zhou, S. Q. Wang and H. M. Liu, Oxazolidinone: A promising scaffold for the development of antibacterial drugs, *Eur. J. Med. Chem.*, 2023, **250**, 115239, DOI: 10.1016/j.ejmech.2023.115239.

9 S. Pathak, P. Singh and G. Jadon, A Review of the Medicinal Importance and Perspectives of the 2-isoxazoline Scaffold, *Med. Chem.*, 2024, **21**(8), 749–760, DOI: 10.2174/0115734064351769241022050641.

10 G. Kumar and R. Shankar, 2-Isoxazolines: A synthetic and medicinal overview, *ChemMedChem*, 2021, **16**(3), 430–447, DOI: 10.1002/cmdc.202000575.

11 E. F. Lopes, F. Penteado, S. Thurow, M. Pinz, A. S. Reis, E. A. Wilhelm, C. Luchese, T. Barcellos, B. Dalberto, D. Alves and M. S. da Silva, Synthesis of isoxazolines by the electrophilic chalcogenation of β, γ-unsaturated oximes: fishing novel anti-inflammatory agents, *J. Org. Chem.*, 2019, **84**(19), 12452–12462, DOI: 10.1021/acs.joc.9b01754.

12 A. Altharawi, M. Enneiymy, Y. Ait Elmachkouri and T. Aldakhil, Synthesis, characterization, DFT, and in-Silico analysis of isoxazole-thiazolidinone hybrids: Reactivity and anticancer potential assessed through pharmacological network, molecular dynamics, molecular docking, and ADMET analysis, *J. Mol. Struct.*, 2025, **1336**, 142088, DOI: 10.1016/j.molstruc.2025.142088.

13 K. Tripathi, P. Kaushik, D. K. Yadav, R. Kumar, S. R. Misra, R. Godara, B. M. Bashyal, V. S. Rana, R. Kumar, J. Yadav and N. A. Shakil, Synthesis, antifungal evaluation, two-dimensional quantitative structure–activity relationship and molecular docking studies of isoxazole derivatives as potential fungicides, *Pest Manage. Sci.*, 2025, **81**(5), 2579–2597, DOI: 10.1002/ps.8152.

14 P. Picconi, P. Prabaharan, J. L. Auer, S. Sandiford, F. Cascio, M. Chowdhury, C. Hind, M. E. Wand, J. M. Sutton and K. M. Rahman, Novel pyridyl nitrofuranyl isoxazolines show antibacterial activity against multiple drug resistant Staphylococcus species, *Bioorg. Med. Chem.*, 2017, **25**(15), 3971–3979, DOI: 10.1016/j.bmc.2017.05.037.

15 A. Alshamari, M. Al-Qudah, F. Hamadeh, L. A. Al-Momani and S. Abu-Orabi, Synthesis, antimicrobial and antioxidant activities of 2-isoxazoline derivatives, *Molecules*, 2020, **25**(18), 4271, DOI: 10.3390/molecules25184271.

16 D. Goyard, B. Kónya, A. S. Chajistamatiou, E. D. Chrysina, J. Leroy, S. Balzarin, M. Tournier, D. Tousch, P. Petit, C. Duret and P. Maurel, Glucose-derived spiro-isoxazolines are anti-hyperglycemic agents against type 2 diabetes through glycogen phosphorylase inhibition, *Eur. J. Med. Chem.*, 2016, **108**, 444–454, DOI: 10.1016/j.ejmech.2015.12.004.

17 S. A. Pandeya, S. Smitha, M. Jyoti and S. K. Sridhar, Biological activities of isatin and its derivatives, *Acta Pharm.*, 2005, **55**, 27–46.

18 P. Pakravan, S. Kashanian, M. M. Khodaei and F. J. Harding, Biochemical and pharmacological characterization of isatin and its derivatives: from structure to activity, *Pharmacol. Rep.*, 2013, **65**(2), 313–335, DOI: 10.1016/S1734-1140(13)71007-7.

19 M. C. Pirrung, S. V. Pansare, K. D. Sarma, K. A. Keith and E. R. Kern, Combinatorial optimization of isatin-β-thiosemicarbazones as anti-poxvirus agents, *J. Med. Chem.*, 2005, **48**(8), 3045–3050, DOI: 10.1021/jm049147h.

20 I. J. Kang, L. W. Wang, T. A. Hsu, A. Yueh, C. C. Lee, Y. C. Lee, C. Y. Lee, Y. S. Chao, S. R. Shih and J. H. Chern, Isatin-β-thiosemicarbazones as potent herpes simplex virus inhibitors, *Bioorg. Med. Chem. Lett.*, 2011, **21**(7), 1948–1952, DOI: 10.1016/j.bmcl.2011.02.037.

21 L. R. Do Valle, P. R. De Melo, L. F. de Salles Gomes and L. M. Proenca, Methisazone in prevention of variola minor among contacts, *Lancet*, 1965, **2**(7420), 976–978, DOI: 10.1016/s0140-6736(65)92840-0.

22 D. J. Bauer and P. W. Sadler, The structure-activity relationships of the antiviral chemotherapeutic activity of isatin β-thiosemicarbazone, *Br. J. Pharmacol. Chemother.*, 1960, **15**(1), 101–110, DOI: 10.1111/j.1476-5381.1960.tb01216.x.

23 M. D. Hall, N. K. Salam, J. L. Hellawell, H. M. Fales, C. B. Kensler, J. A. Ludwig, G. Szakacs, D. E. Hibbs and M. M. Gottesman, Synthesis, activity, and pharmacophore development for isatin-β-thiosemicarbazones with selective activity toward multidrug-resistant cells, *J. Med. Chem.*, 2009, **52**(10), 3191–3204, DOI: 10.1021/jm800861c.

24 F. Degola, C. Morcia, F. Bisceglie, F. Mussi, G. Tumino, R. Ghizzoni, G. Pelosi, V. Terzi, A. Buschini, F. M. Restivo and T. Lodi, In vitro evaluation of the activity of thiosemicarbazone derivatives against mycotoxigenic fungi affecting cereals, *Int. J. Food Microbiol.*, 2015, **200**, 104–111, DOI: 10.1016/j.ijfoodmicro.2015.02.009.

25 M. Enneiymy, H. A. Mohammad-Salim, A. Oubella, J. V. de Julián-Ortiz, H. M. Tsahnang Fofack, S. A. Alotaibi, M. M. Mbake and M. Y. Ait Itto, In-silico analysis of benzo-selenadiazole hybrids: reactivity and anticancer potential assessed through DFT, molecular dynamics, molecular docking, and ADMET, *Polycyclic Aromat. Compd.*, 2025, **45**(8), 1536–1558, DOI: 10.1080/10406638.2025.2470274.

26 A. Oubella, M. Y. Ait Itto, A. Auhmani, A. Riahi, A. Robert, J. C. Daran, H. Morjani, C. A. Parish and M. H. Esseffar, Diastereoselective synthesis and cytotoxic evaluation of new isoxazoles and pyrazoles with monoterpenic skeleton, *J. Mol. Struct.*, 2019, **1198**, 126924, DOI: 10.1016/j.molstruc.2019.126924.

27 O. Y. Celiktas, E. H. Kocabas, E. Bedir, F. V. Sukan, T. Ozek and K. H. Baser, Antimicrobial activities of methanol extracts and essential oils of Rosmarinus officinalis, depending on location and seasonal variations, *Food Chem.*, 2007, **100**(2), 553–559, DOI: 10.1016/j.foodchem.2005.10.011.

28 M. C. Pellegrini, L. Zalazar, S. R. Fuselli and A. G. Ponce, Inhibitory action of essential oils against proteases activity of Paenibacillus larvae, the etiological agent of American Foulbrood disease, *Spanish J. Agric. Res.*, 2017, **15**(4), e0504, DOI: 10.5424/sjar/2017154-10785.

29 A. Daina, O. Michielin and V. Zoete, SwissTargetPrediction: Updated data and new features for efficient prediction of protein targets of small molecules, *Nucleic Acids Res.*, 2019, **47**(W1), W357–W364, DOI: 10.1093/nar/gkz382.

30 N. Rappaport, M. Twik, I. Plaschkes, R. Nudel, T. Iny Stein, J. Levitt, M. Gershoni, C. P. Morrey, M. Safran and D. Lancet, MalaCards: an amalgamated human disease compendium with diverse clinical and genetic annotation and structured search (PMID: 27899610; Citations: 531), *Nucleic Acids Res.*, 2016, **45**(D1), D877–D887, DOI: 10.1093/nar/gkw1012.

31 H. Heberle, G. V. Meirelles, F. R. da Silva, G. P. Telles and R. Minghim, InteractiVenn: A web-based tool for the analysis of sets through Venn diagrams, *BMC Bioinf.*, 2015, **16**(1), 169, DOI: 10.1186/s12859-015-0611-3.

32 G. Dennis, B. T. Sherman, D. A. Hosack, J. Yang, W. Gao, H. C. Lane and R. A. Lempicki, DAVID: Database for annotation, visualization, and integrated discovery, *Genome Biol.*, 2003, **4**(9), R60, DOI: 10.1186/gb-2003-4-9-r60.

33 M. Franz, C. T. Lopes, D. Fong, M. Kucera, M. Cheung, M. C. Siper, G. Huck, Y. Dong, O. Sumer and G. D. Bader, Cytoscape.js 2023 update: A graph theory library for visualization and analysis, *Bioinformatics*, 2023, **39**(1), 1–3, DOI: 10.1093/bioinformatics/btad031.

34 D. Szklarczyk, A. L. Gable, K. C. Nastou, D. Lyon, R. Kirsch, S. Pyysalo, N. T. Doncheva, M. Legeay, T. Fang, P. Bork, L. J. Jensen and C. von Mering, The STRING database in 2021: Customizable protein–protein networks, and functional characterization of useruploaded gene/measurement sets, *Nucleic Acids Res.*, 2021, **49**(D1), D605–D612, DOI: 10.1093/nar/gkaa1074.

35 C. A. Lipinski, F. Lombardo, B. W. Dominy and P. J. Feeney, Experimental and computational approaches to estimate solubility and permeability in drug discovery and development settings, *Adv. Drug Deliv. Rev.*, 1997, **23**(1–3), 3–25, DOI: 10.1016/S0169-409X(96)00423-1.

36 A. Daina, O. Michielin and V. Zoete, SwissADME: a free web tool to evaluate pharmacokinetics, drug-likeness and medicinal chemistry friendliness of small molecules, *Sci. Rep.*, 2017, **7**, 1–13.

37 P. Banerjee, A. O. Eckert, A. K. Schrey and R. Preissner, ProTox-II: a webserver for the prediction of toxicity of chemicals, *Nucleic Acids Res.*, 2018, **46**(W1), W257–W263, DOI: 10.1093/nar/gky318.

38 G. Krishnu, G. Paleti, B. K. Chagaleti, A. Mueen and S. Balakrishnan, Design, Synthesis and Evaluation of Substituted Benzimidazoles as Potent Polyketide Synthase 13 Inhibitors for Tuberculosis, *J. Young Pharm.*, 2025, **17**(1), 149.

39 G. M. Morris, R. Huey, W. Lindstrom, M. F. Sanner, R. K. Belew, D. S. Goodsell and A. J. Olson, Autodock4 and AutoDockTools4: automated docking with selective receptor flexiblity, *J. Comput. Chem.*, 2009, **16**, 2785–2791.

40 E. F. Pettersen, T. D. Goddard, C. C. Huang, G. S. Couch, D. M. Greenblatt, E. C. Meng and T. E. Ferrin, "UCSF Chimera - A Visualization System for Exploratory Research and Analysis", *J. Comput. Chem.*, 2004, **25**(13), 1605–1612.

41 D. S. Biovia, *Discovery Studio Visualizer*, San Diego, 2021.

42 B. A. Velmurugan, B. Sivaraman and R. Natarajan2D Qsar and Docking Studies on Chalcone-Quinoxaline Variants–a Potential Target for Acetylcholinestrase Inhibitors, Preprint(Version 1) available at Research Square, 2023, DOI: 10.21203/rs.3.rs-2957048/v1.

43 A. Sadula, B. K. Chagaleti, M. Enneiymy, U. R. Peddaboina, A. Ankireddy, M. F. Al Ajmi and A. Oubella, Multifaceted Analysis of Novel Trisubstituted Imidazole Chromen Derivatives: Design, Synthesis, Characterization, Molecular

docking, and Antimicrobial Evaluation, *J. Mol. Struct.*, 2025, **1**, 143185.

44 B. K. Chagaleti, B. S. Kumar, R. Rajagopal, A. Alfarhan, J. Arockiaraj, K. M. Kumaradoss and S. K. R. Namasivayam, Targeting cyclin-dependent kinase 2 CDK2: Insights from Molecular Docking and Dynamics Simulation-A systematic computational approach to discover novel cancer therapeutics, *Comput. Biol. Chem.*, 2024, 108134.

45 S. Genheden and U. Ryde, The MM/PBSA and MM/GBSA methods to estimate ligand-binding affinities, *Expert Opin. Drug Discov.*, 2015, **10**(5), 449–461.

46 S. M. Bellapukonda, S. Singothu, A. Singampalli, R. Bandela, P. Kumar, V. M. Yaddanapudi, V. Bhandari, S. Nanduri, M. Enneiymy and M. F. AlAjm, Exploring spirocyclic isoquinoline-piperidine compounds in tuberculosis therapy: ADMET profiling, docking, DFT, MD simulations, and MMGBSA analysis, *Comput. Biol. Chem.*, 2025, **118**, 108447.

47 B. Sivaraman and M. K. Kathiravan, Targeting Aurora A Kinase: Computational Discovery of Potent Inhibitors through Integrated Pharmacophore and Simulation Approaches, *Comput. Biol. Chem.*, 2025, **17**, 108690.

48 B. Sivaraman, L. Maji, B. K. Chagaleti and K. Muthukumaradoss, Exploration of a Novel Imidazo [4, 5-b] pyridine–dihydropyrimidinone hybrids as aurora kinase a inhibitors: integrated pharmacophore modelling, docking and simulation approaches, *Mol. Diversity*, 2026, **10**, 1–22.

49 O. Afzal, M. Enneiymy, S. Bibi, H. A. Madkhali, T. Aldakhil, B. K. Chagaleti, S. G. Khan, Y. Riadi, A. Altharawi and R. A. Haggam, Design, synthesis and computational evaluation of 1, 2, 3-triazole-Schiff base hybrid as AKT1 inhibitor for breast cancer, *Chem. Phys. Impact*, 2026, 101001.